Korean Journal of Chemical Engineering
https://doi.org/10.1007/s11814-024-00279-y

REVIEW ARTICLE (INVITED ONLY)

Synthesis Strategies and Applications of Non-toxic Quantum Dots

Yunmo Sung[1] · Jaewon Chang[2] · Sukyung Choi[1] · Sanghwa Jeong[2]

Received: 18 June 2024 / Revised: 18 June 2024 / Accepted: 5 September 2024

Abstract
This review provides an in-depth analysis of the latest non-toxic quantum dot (QD) synthesis strategies and their applications in optoelectronics and biomedical engineering. In addition, this review presents the development of synthetic approaches for non-heavy metal QDs that retain the desirable photophysical properties of their traditional counterparts while reducing their potential toxicity. We highlight the pivotal role of non-toxic QDs in advancing display technologies, focusing on their contribution to improving color purity and brightness in next-generation screens. In the biomedical field, applications of non-toxic QDs in bio-imaging, bio-sensing, and targeted drug delivery have been elaborated, emphasizing their enhanced biocompatibility and utility in precise diagnostics and therapeutics. The authors present insights and challenges underlining the transformative potential of non-toxic QDs for high-resolution display devices and advanced biomedical solutions to improve their functional attributes and safety for practical use.

Keywords Quantum dot · Non-toxic · Eco-friendly · Synthesis · Display · Bio-application

Introduction

Quantum dots (QDs) are semiconductor nanocrystals with sizes of 1–100 nm, containing hundreds to thousands of atoms and covered with organic surfactant molecules called "ligands," which show size-dependent discrete electronic transitions [1]. Conventional bulk semiconductors exhibit optoelectronic properties primarily determined by their material composition, crystal structure, and dopants [2]. When the size of the semiconductor is within the exciton Bohr diameter, i.e., finite size of excitons in the crystal, charge carriers become spatially confined. This quantum-confined structure exhibits size-dependent optoelectronic properties, leading to additional degrees of tunability compared to bulk semiconductors [1, 2]. As the QDs become smaller, quantum confinement increases the effective bandgap and results in a blue shift in the absorption and emission profiles, enabling the design of QDs with ultraviolet (UV), visible, near-infrared (NIR), and mid-infrared spectral ranges. When an electron in the valence band is excited to the conduction band, it interacts strongly with the valence band holes, such as Coulomb and spin-exchange interactions, exhibiting a unique optoelectronic structure [2, 3]. In particular, under high excitation energies, multiple excitons can accumulate in a QD, leading to enhanced many-body phenomena, such as the Stark effect, Auger recombination, and amplified spontaneous emission, affecting the optical and electronic properties of QD [3].

QD synthesis can be categorized into bottom–up and top–down methods. Top–down physical methods rely on lithography or milling to define the nanometer-sized volume of an existing semiconductor. In bottom–up methods, QDs are initially synthesized using layer-by-layer crystal growth techniques, such as molecular beam epitaxy (MBE) and chemical vapor deposition (CVD), which produce highly crystalline Si and III-V semiconductors with tunable optoelectronic properties [2]. Currently, bottom–up synthetic methods for colloidal QDs in solution have been reported, resulting in a variety of QDs [e.g., CdSe, ZnTe, HgSe, PbS, InP, Ag_2S, $CuInS_2$, and $Ag(InGa)S_2$] with absorption/emission wavelengths ranging from the UV to the NIR region, narrow luminescence full-width at half maximum (FWHM),

✉ Sukyung Choi
skchoi915@etri.re.kr

✉ Sanghwa Jeong
sanghwa.jeong@pusan.ac.kr

[1] Reality Device Research Division, Electronics and Telecommunications Research Institute (ETRI), Daejeon 34129, Republic of Korea

[2] School of Biomedical Convergence Engineering, Pusan National University, Yangsan 50612, Republic of Korea

Published online: 16 September 2024

high stability, and near-unity luminescence quantum yield (QY) [4, 5]. These high-quality QDs, especially those with high color purity and durability, combined with their solution processability, have enabled the rapid growth of QD applications, such as bio-imaging/medicine, energy harvesting devices, quantum information, and displays [2, 6, 7]. However, the enforcement of the restriction of hazardous substances directive (RoHS) by the European Union prohibited the sale of products containing more than 0.01 wt% of Cd. Consequently, developing environmentally friendly QDs free from toxic heavy metals, such as Cd, Hg, and Pb, has gained considerable interest, particularly with the emerging need for non-toxic QDs. In particular, non-toxic QDs are in high demand for bio-applications and display applications that have the potential to be utilized in our daily lives, addressing concerns related to cytotoxicity and environmental impact.

In this review, we present an overview of the synthesis of non-toxic QDs and their bio- and display applications. First, we introduce the synthetic methods for a variety of non-toxic QDs, including indium pnictides, silver chalcogenides, I–III–VI ternary/quaternary QDs, and zinc chalcogenides. In the following sections, display applications are reviewed, starting with an introduction to the QD display market and finishing with QD technologies currently being applied to displays, such as QD color-conversion layers, QLED, and micropatterning. The non-toxic visible QDs mainly introduced in this section belong to the indium pnictides and I–III–VI groups, which are currently commercialized or under development. Next, the bio-applications of non-toxic QDs are discussed, focusing on recent progress in the fields of bio-sensing, in vivo imaging, and drug delivery. This section describes NIR-emitting Ag- or Cu-based QDs, Mn-doped Zn chalcogenide QDs, and blue-emitting InP QDs.

Synthetic Methodologies of Non-toxic QDs

Indium Pnictides

InP

Indium phosphide (InP) QDs are direct band-gap semiconductors with a bulk bandgap of 1.35 eV that can be emitted from the blue (~465 nm) to the NIR (~750 nm) region by simply tuning their size. InP QDs have relatively lower toxicity than Cd-based QDs and thus have the potential to be used commercially, especially in displays. Colloidal InP QDs were first synthesized by the reaction of $InCl_3$ and tris(trimethylsilyl)phosphine ($P(TMS)_3$) in trioctylphosphine oxide (TOPO) at 270–360 °C for 72 h [8]. This reaction is based on the decomposition of $P(TMS)_3$ by Wells' dehalosilylation reaction, making it the most commonly used phosphorus source for the synthesis of InP QDs [9]. A highly electron-donating silyl group can make phosphorus more Lewis-basic. In this reaction, the Lewis acid $InCl_3$ reacts with the Lewis base, $P(TMS)_3$ to produce highly crystalline InP QDs. However, they have a broad size distribution of ~20% and a poor photoluminescence QY (PLQY) of less than 1%. A non-coordinating solvent, specific fatty acids with well-defined chain lengths, a well-controlled indium-to-ligand ratio, and surface treatment are all critical factors for the successful synthesis of high-quality InP QDs. Peng et al. used 1-octadecene (ODE) as a non-coordinating solvent in the synthesis of InP QDs instead of TOPO [10]. $In(OAc)_3$ and $P(TMS)_3$ were used as precursors. Fatty acids with different chain lengths, amines, phosphines, phosphine oxides, and phosphonic acids were also tested as ligands for ODE. Among all the ligands tested, palmitic acid (PA) and myristic acid (MA) were found to be the best ligands in the ODE solvent when the In:ligand molar ratio in the solution was 1:3. The best as-synthesized InP QD was 3.1 nm with a narrow size distribution of 4.7%; however, the PL QY did not reach a high value. Surface treatment of InP QDs with HF drastically improved the PL QY by as much as ~40% at room temperature [11]. The mechanism of HF treatment is based on removing unpassivated P atoms, which induces trap states within the bandgap of the InP QD and is responsible for the low initial PL QY. Alternatively, the growth of a wide-bandgap inorganic shell on the InP core was also developed to improve the QY, chemical properties, and photostability. Despite the 7.7% lattice mismatch between the InP core and the ZnS shell, ZnS is the most widely used shell material for InP QDs. Weller et al. synthesized InP/ZnS core/shell QDs with a maximum QY of 20% using bistrimethylsilylsulfide ($(TMS)_2S$) and diethyl zinc (Et_2Zn) as ZnS shell precursors [12]. To reduce the lattice mismatch between the InP core and shell materials, Lim et al. successfully used ZnSe (lattice mismatch 3. 3%) as a lattice adaptor between the InP core and ZnS outer shell, allowing for higher shell thicknesses (~1.9 nm) and improved photochemical stability [13]. Recently, the optimized synthesis of a red-emitting InP/ZnSe/ZnS core/shell system with a composition gradient shell, in addition to HF treatment, resulted in a PL QY greater than 90% and an FWHM of 35–36 nm at 620–630 nm [14, 15]. The InP core was treated with HF before shell overcoating; the ZnSe shell was coated with $Zn(OAc)_2$ and trioctylphosphine selenium (TOP-Se) at 340 ℃, and the ZnS shell was coated by adding $Zn(OAc)_2$ and trioctylphosphine sulfur (TOP-S) at the same temperature, resulting in a QD size of 11 nm (Fig. 1a). Currently, green- and red-emitting InP QDs exhibit high QY and stability, but there are still limitations to the synthesis of small blue-emitting InP QDs. The fabrication of highly luminescent blue-emitting InP QDs is not an easy task in QD

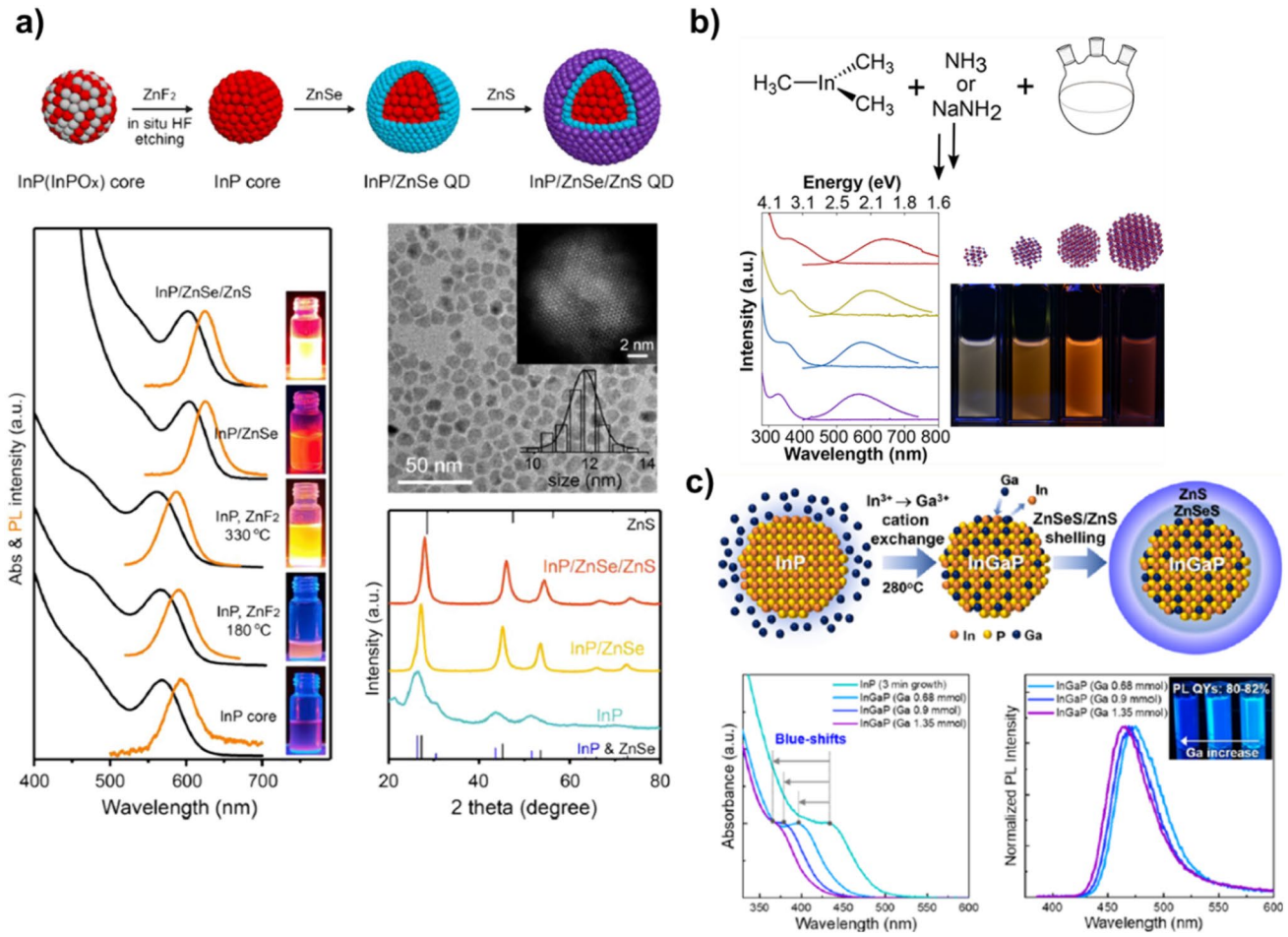

Fig. 1 **a** Schematic of the synthesis of highly luminescent InP/ZnSe/ZnS QDs with HF and their absorption/PL spectra, TEM image, and XRD pattern during QDs synthesis. Inset: corresponding HR-STEM image and size distribution histogram. Reproduced with permission [15]. Copyright 2022 American Chemical Society. **b** Synthetic schematic of high crystalline InN QDs with PL property, and their absorption/PL spectra and photographs with PL at 525, 565, 625, and 680 nm from left to right, illuminated with a 365 nm UV lamp. Adapted from [21]. Copyright 2023 American Chemical Society. **c** Schematic illustration of InGaP core and subsequent ZnSeS/ZnS double shelling and their absorption/PL spectra. Adapted from [25]. Copyright 2020 American Chemical Society

research because of the necessity of an ultrasmall QD core (< 2 nm). Ultrasmall QDs are prone to contain more crystal defects that could affect their luminescence properties, which require improved synthesis strategies. In addition, the highly covalent nature of the InP QDs makes them more susceptible to oxidizing environments. In addition, the commonly used $P(TMS)_3$ is too reactive, leading to inseparable nucleation and growth steps. Therefore, attempts have been made to replace $P(TMS)_3$ with new, less reactive precursors such as tris(trimethylgermyl)phosphine, phosphine (PH_3), aminophosphine, and triphenylphosphite (TPP) for the synthesis of small-sized InP QDs[16].

InN

The fundamental bandgap of InN is thought to be 1.9 eV. However, recent studies on higher quality films of this material have clearly shown that the true value of its direct bandgap is 0.8 eV [17] making it a promising compound for optoelectronic applications, including solid-state lighting, biological imaging, and photovoltaic devices. In the quantum-confinement regime, the bandgap can be further tuned by changing the size and shape of the QDs from visible to NIR, resulting in a large Bohr radius of 8 nm. Several wet chemical synthesis strategies, such as solvothermal synthesis, precursor thermolysis, and dehalosilylation reactions using $N(TMS)_3$ have been used to obtain nanosized InN in colloidal form. The solvothermal method involves synthesis in an autoclave at an elevated pressure. Bai et al. synthesized InN with a size of 28 nm by autoclaving Li_3N and $InCl_3$ in xylene at 250 °C for 24 h [18]. Crystalline InN has also been synthesized by autoclaving InI_3 with $NaNH_2$ in benzene at various temperatures, resulting in InN with a diameter of 10–35 nm [19]. These

high-pressure solvothermal reactions in an autoclave, designed to maximize the formation of crystalline InN, result in products that are not colloidally stable and lack PL. Other attempts to synthesize InN QDs include the thermal decomposition of precursors and dehalosilylation reactions between $InCl_3$ and $N(TMS)_3$ in a non-coordinating solvent using myristic acid as a ligand [20]. However, this method resulted in polydisperse InN and failed to produce fluorescent InN. Recently, both gaseous ammonia (NH_3) and $NaNH_2$ produced monodisperse InN QDs when the organometallic precursor trimethylindium (TMIn), which has a much higher reactivity than indium halide salts, was used as the indium source (Fig. 1b) [21]. The reactions followed the usual hot injection method at 120–180 °C and took place under nitrogen in a high-boiling solvent [hexadecane, squalane, or oleylamine (OAm)]. Depending on the reaction temperature and time, the resulting InN QDs had a size of 5–15 nm and PL characteristics in the range of 475–750 nm, attributed to the presence of InN surface states. However, further investigation is required to optimize the synthesis methods and determine the origin of PL.

InGaP

Ga was synthetically introduced into InP QD, resulting in either a GaP inner shell or an InGaP alloy core. In particular, the development of InGaP alloy QDs is noteworthy, because they can emit blue light and their size is larger than that of binary InP, potentially allowing the reproducible synthesis of bright blue-emitting InGaP QDs. The formation of InGaP QDs, although limited, has been realized either by annealing the grown InP QDs in the presence of a Ga precursor or by cation exchange of the pre-synthesized InP QDs with Ga ions. Reiss et al. reported the comparative heat-up synthesis of InGaP QDs in the presence of Ga acetylacetonate ($Ga(acac)_3$) [22]. The resulting InGaP alloy QDs exhibited a PL maximum of 475 nm and poor QY of 20%, even after ZnS sheathing. Cation exchange is a useful strategy for finely and extensively tuning the composition of pre-synthesized QDs. While cation exchange can easily proceed in ionic bond-dominated II–VI semiconductors, more covalent III–V semiconductors such as In or Ga pnictides are resistant to cation exchange. Therefore, Ga^{3+} cation exchange on pre-grown InP QDs usually occurs near the QD surface, resulting in an InP/GaP core/shell form [23]. In an effort to induce more extensive Ga alloying of InP QDs, cation exchange was performed in molten salt at high temperatures of 380–450 °C [24]. These successfully alloyed $In_{0.5}Ga_{0.5}P$ QDs exhibited a tunable emission range of 495–640 nm with moderate QYs of 30–40% after ZnS shelling. Yang et al. reported the synthesis of blue-emitting ternary InGaP QDs via In^{3+} to Ga^{3+} cation exchange at a relatively low temperature of 280 °C (Fig. 1c) [25]. The degree of Ga alloying in the InP core host was systematically controlled by varying the amount of GaI_3 added. The cation-exchanged InGaP cores were then double-shelled with ZnSeS inner and outer shells. The resulting InGaP/ZnSeS/ZnS QDs exhibited tunable blue emissions in the range of 465–475 nm, depending on the degree of Ga alloying. Among the series of QD samples, the optimal blue QDs had a PL peak at 465 nm and a QY of 80%.

Silver Chalcogenides

Ag_2S

Monoclinic α-Ag_2S, with a bulk bandgap of 1.1 eV and a relatively large absorption coefficient, has been used as building blocks for NIR LEDs, photodetectors, and solar cells. In addition, Ag_2S has been reported to have negligible toxicity to organisms; therefore, NIR-emitting Ag_2S QDs have potential applications in biomedical imaging devices. Wang et al. [26] first synthesized NIR-emitting single-crystalline monodispersed Ag_2S QDs using a single-source precursor of silver diethyldithiocarbamate [Ag(DDTC)] with oleic acid (OA), octadecylamine (ODAm), and ODE. The as-synthesized Ag_2S QDs with a size of 10.2 nm (beyond the exciton Bohr diameter of 4.4 nm) exhibited NIR emission at 1058 nm under 785 nm excitation (Fig. 2a). The same team reported that, based on the decomposition of Ag-DDTC in neat dodecanethiol (DDT), variations in the reaction temperature and reaction time allowed the modulation of the size of Ag_2S QDs (Fig. 2a) [27]. The diameter gradually increased from 2.4 to 7 nm and the NIR PL shifted from 915 to 1175 nm. The sizes of Ag_2S QDs were also controlled by varying the Ag/S ratio [28]. The seeds of Ag_2S QDs are rich in silver, and a higher Ag/S ratio results in a larger number of nuclei, yielding a smaller QD size. Doh et al. reported that varying the Ag/S ratio from 100 to 1/100 tuned the size of Ag_2S QD size from 2.8 to 14.4 nm [29]. They used sulfur in toluene as the S precursor, and $AgNO_3$ in octylamine and toluene as the Ag precursor. The size of the as-synthesized Ag_2S QDs covered a range of PL wavelengths from 1000 to 1200 nm. However, the Ag_2S QDs exhibited poor PL properties, probably because of the large number of Ag vacancies induced by the low lattice energy. The passivation of the QD surface with thick and robust inorganic shells suppresses the surface trap states. For example, the coating of the ZnS shell on the Ag_2S QDs has been applied to reduce surface defects. However, these methods failed to achieve a high PLQY owing to the large lattice mismatch (approximately 16%) between the Ag_2S core and the ZnS shell. Alternatively, the robust binding of ligands to the surface atoms of QDs can inhibit non-radiative recombination, resulting in a high PLQY. Recently, NIR-II-emissive Ag_2S QDs with a PLQY of 47.6% were synthesized via chloride-mediated

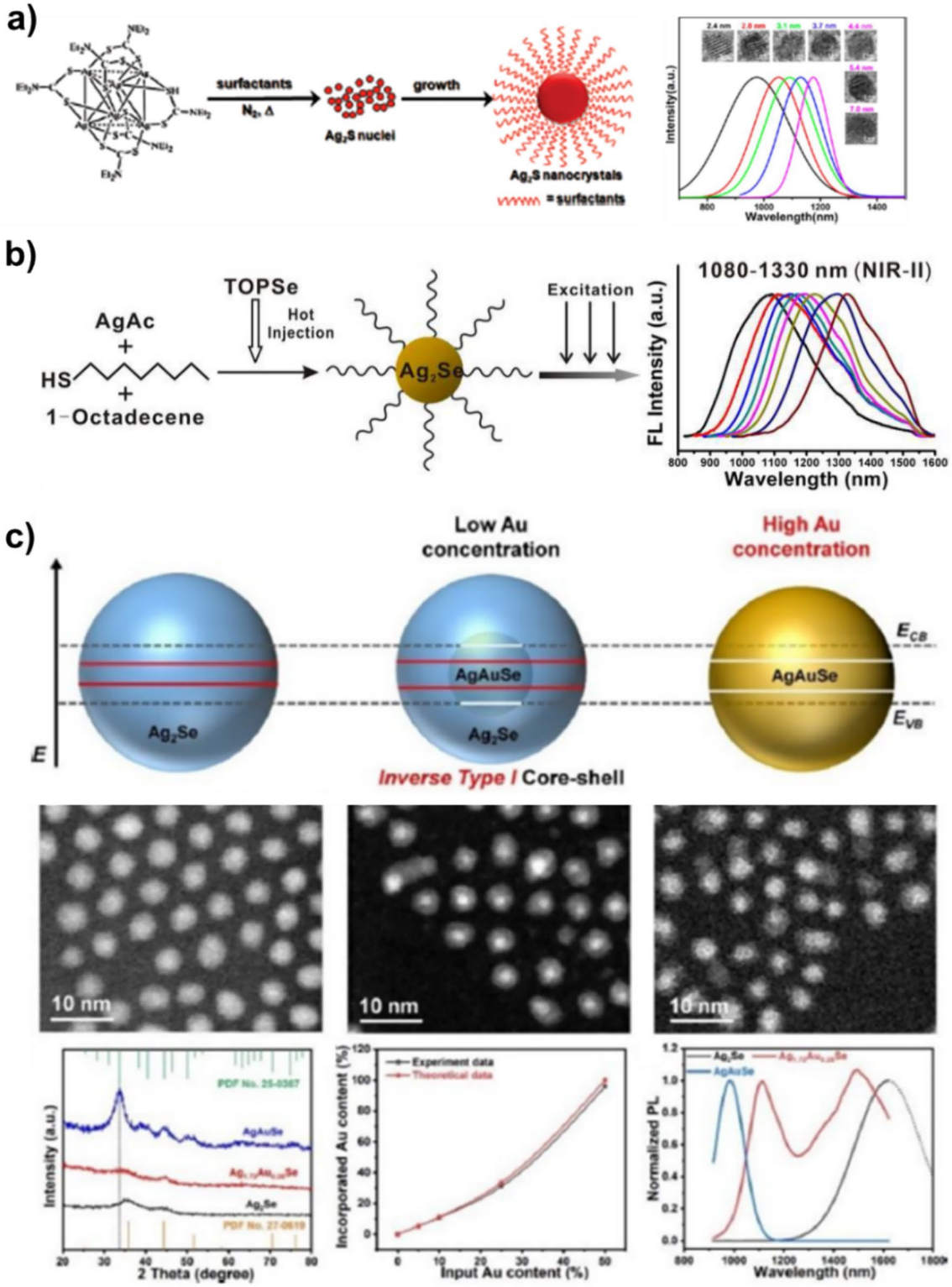

Fig. 2 **a** Schematic of the synthesis of Ag_2S NIR QDs from a single-source precursor of Ag(DDTC) and their size-dependent TEM images and PL spectra. Reproduced with permission [26, 27]. Copyright 2010/2014 American Chemical Society. **b** Strategy for preparing Ag2Se QDs with tunable emission in the NIR-II window and PL spectra of the as-prepared Ag_2Se QDs. Adapted from [33]. Copyright 2013 American Chemical Society. **c** Schematic diagram of structure evolution of AgAuSe alloy QDs, with the HAADF-STEM images, XRD pattern, and elemental analysis showing the amount of Au incorporated into the Ag_2Se QDs relative to the ratio of Au/Ag added to the reaction solution and PL transformation. Reproduced with permission [37]. Copyright 2021 American Chemical Society

growth and passivation. Ag(OAc) in OAm, OA, ODE, and Na_2S aqueous solutions were used as the Ag and S precursors, respectively [30]. After the reaction of two solutions, as-synthesized Ag_2S QDs were dispersed in tetrachloroethylene (TCE) and heated to 115 ℃. TCE can decompose into chloride ions at 115 ℃ and act as a source of chloride ligands. These chloride ligands contributed to the replacement of organic ligands and decreased the density of the surface dangling bonds, resulting in a high PLQY. In addition, Kim et al. reported that stoichiometric Ag_2S QDs exhibited a PL intensity more than ten times when that of nonstoichiometric Ag_2S QDs [31]. The addition of ion-pair cetyltrimethylammonium sulfide (CTAS) ligands to silver-rich Ag_2S QDs produced stoichiometric Ag_2S QDs with greatly enhanced PLQY.

Ag_2Se

Ag_2Se has a narrow direct bandgap of 0.15 eV for bulk materials and exhibits excellent PL properties in the NIR-II window. In the quantum-confinement regime with diameters of < 5.8 nm (exciton Bohr radius of 2.9 nm), less-toxic Ag_2Se QDs are promising alternatives to NIR-II-emitting nanoprobes. The first demonstration of monodisperse, spherical Ag_2Se QDs synthesis was reported by Norris et al. [32]. Ag_2Se QDs were synthesized by the hot injection of TOP-Ag and TOP-Se into ODE, ODAm, and OA, but they did not exhibit PL properties. To improve the PL properties by surface passivation of Ag_2Se QDs, Tian et al. used 1-octanethiol (OT) as a capping ligand to efficiently balance the nucleation and growth processes of the QDs (Fig. 2b) [33]. According to the hard and soft acid and base theory, the thiol functional group is a soft base and Ag is a soft acid; therefore, they can form strong complexes with each other. They used silver acetate [Ag(OAc)] and TOP-Se as precursors and ODE as the solvent. The prepared Ag_2Se QDs showed tunable PL in the NIR-II biological window ranging from 1080 to 1330 nm with a PLQY of 9.58% but did not exhibit distinct absorption features, probably because of the broad size distribution. The same group switched from TOP-Se to ODE-Se to synthesize homogeneous Ag_2Se QDs by increasing the reactivity of the Se precursor [34]. As the sizes of Ag_2Se QDs increased from 1.9 to 3.1 nm, the exciton absorption peaks shifted from 830 to 954 nm, and the PL emission varied from 958 to 1020 nm with PLQY up to 23.4%. Dong et al. prepared Ag_2Se QDs with a narrow size distribution using reactive NaHSe as the Se precursor [35]. In this synthesis, a solution of $AgNO_3$ dissolved in OAm/toluene was reacted with DDT and NaHSe for 1 h at 180 ℃. The resulting Ag_2Se QDs exhibited PL at 1300 nm with a high PLQY of 29.4%. To further improve the PL properties of Ag_2Se QDs, Yarema et al. reported a synthesis route for Ag_2Se/ZnSe core/shell QDs that increased the PL intensity by 40%, with better stability than that of Ag_2Se QDs [36]. In this reaction, $Zn(OAc)_2$ dissolved in OAm was injected into the as-synthesized Ag_2Se QDs containing excess Se, and the resulting Ag_2Se/ZnSe QDs increased in size from 2.0 to 2.2 nm.

AgAuSe or AgAuS

In the case of Ag_2Se and Ag_2S, the high mobility of the Ag ions leads to numerous cation vacancies and crystal defects, resulting in a low PLQY of less than 1%. An alternative strategy for improving the optical properties of QDs is the synthesis of AgAuSe or AgAuS QDs. The AgAuSe QDs were first reported by Wang et al. [37] prepared alloyed AgAuSe QDs by incorporating pre-synthesized Ag_2Se QDs with Au precursors using the cation-exchange method (Fig. 2c). First, Ag_2Se QDs with diameters of 4.58 nm were synthesized. Ag(OAc) dispersed in OAm and DDT were used as the Ag source. Then, the mixture was heated to 170 ℃ and tributylphosphine selenide (TBP-Se) was injected into the reaction solution. $HAuCl_4$-$3H_2O$ dissolved in chloroform and OAm were then added to the Ag_2Se QDs solution to form alloyed AgAuSe QDs. OAm is known for its ability to reduce the metallic nanoparticles. Thus, Au(III) can be reduced to Au(I) by OAm, and Au(I) can be exchanged for Ag(I) in the Ag_2Se QDs, resulting in alloyed AgAuSe QDs. These processes occur at room temperature with extremely short and moderate reaction times. A low energy barrier is associated with these processes and the high thermodynamic stability of fischesserite and AgAuSe. The As-synthesized Ag_2Se QDs emitted at 1610 nm and showed a very low PLQY, whereas the alloyed AgAuSe showed a high PLQY of 65.3% at 978 nm. The PLQY of the alloyed AgAuSe QDs contributes to the optical properties of the parent Ag_2Se QDs. The effect of aliphatic chain length on the optical properties of Ag_2Se QDs was investigated by selecting OT, DDT, and hexadecanethiol (HDT) as capping ligands [38]. The shortest OT ligand was found to be ideal for the synthesis of high-quality Ag_2Se QDs compared to DDT and HDT, owing to its excellent passivation ability for surface defects. By alloying high-quality parent OT-capped Ag_2Se QDs with an Au^+ precursor, nearly trap-free AgAuSe QDs with a record absolute PLQY of 87.2% at 970 nm were obtained. The AgAuSe QDs had diameters in the range of 5–15 nm, and size modulation was achieved by changing either the temperature or the growth time. AgAuS QDs were prepared using a cation-exchange method based on alloyed AgAuSe QDs. Yang et al. synthesized Ag_2S QDs using $AgNO_3$ and 3-mercaptopropionic acid (MPA) in water [39]. MPA acts as a surface ligand and sulfur source. AgAuS QDs were then obtained by reacting the Ag_2S QDs with $HAuCl_4$. The prepared AgAuS QDs exhibited uniform dispersion with a diameter of 2.3 nm and a PL QY of 34.91% at 707 nm. The

PL wavelengths of the AgAuS QDs with different molar ratios of Au and Ag (0.01:1, 0.1:1, 0.5:1, and 1:1) showed an orderly red shift from 584 to 707 nm.

I-III-VI QDs

$AgInS_2$

Ternary $AgInS_2$ (AIS) materials exhibit a direct bandgap from the visible to the NIR region, with band gaps of 1.87 eV. They usually crystallize in a chalcopyrite tetragonal structure and can be considered zinc-blende type. The cations (Ag^+ and In^{3+}) were stacked alternately, and each cation was tetrahedrally coordinated with four anions (S^{2-}). At high temperatures or at the nanoscale, AIS can be transformed into an orthorhombic crystal structure similar to a tetragonal structure. Orthorhombic AIS has a direct bandgap of about 1.98 eV in bulk. One phase of ternary AIS is an in-rich compound with the general formula $AgIn_5S_8$, which has a cubic spinel structure and a bulk bandgap of 1.80 eV. At the nanoscale, the synthesis of metastable cubic $AgIn_5S_8$ can be prepared by adjusting the stoichiometric Ag/In ratio at reaction temperatures ranging from 120 to 180 ℃ [40]. To prepare general tetragonal or orthorhombic AIS QDs, metal-DDTC ($M(DDTC)_x$), DDT, thiourea, and elemental sulfur dissolved in OAm or ODE are the main sulfur sources. The initial tetragonal AIS QDs were synthesized using M(DDTC)x. Heating AgDDTC, $In(DDTC)_3$, and $Zn(DDTC)_2$ in OAm caused the thermal decomposition of the precursors and produced AIS/ZnS QDs, which consisted of an alloyed ZnS-AIS core and outer ZnS shell [41]. The PL wavelength of the AIS/ZnS QDs was controlled by changing the ratio of the metal ions in the range 500–800 nm, with a maximum PLQY of ~ 80%. High Ag(In)/Zn and Ag/In ratios resulted in red-shifted PL peaks. The soft Lewis base DDT efficiently complexes with the soft Lewis acid Ag^+ as a stabilizing agent and acts as a sulfur source. Using $AgNO_3$ and $In(OAc)_3$ in the heating synthesis, DDT was mixed with ODE, and oleic acid and TOP were introduced as additional complexing agents for In^{3+} and Ag^+, resulting in orthorhombic AIS QDs with a size of 2.5 nm (Fig. 3a) [42]. The as-synthesized orthorhombic AIS QDs were overcoated with ZnS shells using $Zn(St)_2$ and elemental sulfur in an OAm/ODE solvent, resulting in a PLQY of over 41% in the range of 520–680 nm. Susumu et al. used thiourea to synthesize tetragonal AIS QDs at mild temperatures [43]. Thiourea starts thermal decomposition at 180 ℃, but the presence of OAm lowers the decomposition temperature of thiourea to below 100 ℃. A mixture of thiourea, $In(OAc)_3$, and Ag(OAc) in OAm and DDT was heated to 140 ℃, resulting in tetragonal AIS QDs. The As-synthesized AIS QDs have a size of approximately 4 nm and a PLQY of 64% at 700 nm. The elemental sulfur in OAm/ODE was used in the hot injection method. In ODE or OAm, the ring-opening reaction of elemental sulfur caused H_2S or ammonium sulfide, which can act as a sulfur source. Peng et al. synthesized AIS QDs by hot injecting OAm-S into a metal precursor pot containing $AgNO_3$, $In(OAc)_3$, OA, DDT, and ODE [44]. The synthesized AIS QDs had a diameter of 3.5 nm and PLQY of 37.8% at 618 nm. Burda et al. reported a one-pot method for the synthesis of AIS/ZnS QDs by hot injecting ODE-S into a mixture of $AgNO_3$, $In(OAc)_3$, $Zn(St)_2$, OA, DDT, TOP, and ODE [45]. However, the prepared AIS/ZnS QDs exhibit a poor PL QY of 8.9% at 602 nm. The high reactivity of the H_2S generated from ODE-S can cause the formation of Ag_2S QDs with low lattice energies; therefore, alloyed AIS QDs may not be fully produced.

$AgInGaS_2$

The $AgInGaS_2$ (AIGS) quaternary system is particularly valuable for various display and lighting applications, because the band gaps of both $AgInS_2$ (~ 1.8 eV) and $AgGaS_2$ (~ 2.6 eV) are in the visible region, and both materials are miscible over a full range of indium/gallium (In/Ga) compositions. The AIGS QDs were synthesized using a one-pot annealing method. Yang et al. prepared AIGS QDs by heating the solution containing AgI, $Ga(acac)_3$, $In(OAc)_3$, elemental sulfur, DDT, and OAm to 240 ℃ [46]. Similar to ternary I-III-VI, the PL wavelength in the range of 540–570 nm was controlled by changing the In/Ga ratio. The ZnS shell was also overcoated on the AIGS core to improve the PLQY using Zn-alkylcarboxylate. The As-synthesized AIGS/ZnS QDs yielded a PLQY of approximately 70% but a very broad PL with an FWHM above 130 nm owing to donor–acceptor recombination. Susumu et al. fabricated AIGS QDs with a narrow PL emission by introducing a GaS_x shell [47]. Low-crystalline GaS_x can be well adsorbed onto the surface of AIGS QDs to passivate surface defects. They prepared the AIGS core by heating Ag(OAc), $In(OAc)_3$, and $Ga(DDTC)_3$ in OAm at 150 ℃, and then, the GaS_x shell was coated on the core using $Ga(acac)_3$ and dimethylthiourea at 280 ℃. As-synthesized AIGS/GaS_x QDs exhibited FWHM of 32–42 nm in the emission region of 500–600 nm with PLQY of 28–59%. However, in the case of the solution containing the Ag precursor together with other precursors, a cloudy dispersion was produced at elevated temperatures owing to the rapid formation of large Ag_2S particles, resulting in a low chemical yield. The same group reported a new approach for synthesizing AIGS QDs by injecting an Ag precursor into In/Ga/S precursors (Fig. 3b) [48]. The Ag precursor injection approach resulted in a clear orange-red solution, rather than a cloudy solution. $InCl_3$, $In(DDTC)_3$, and $Ga(DDTC)_3$ in OAm were used as the In/Ga/S precursors, and Ag(OAc) in OAm as Ag precursor was injected into a solution of the

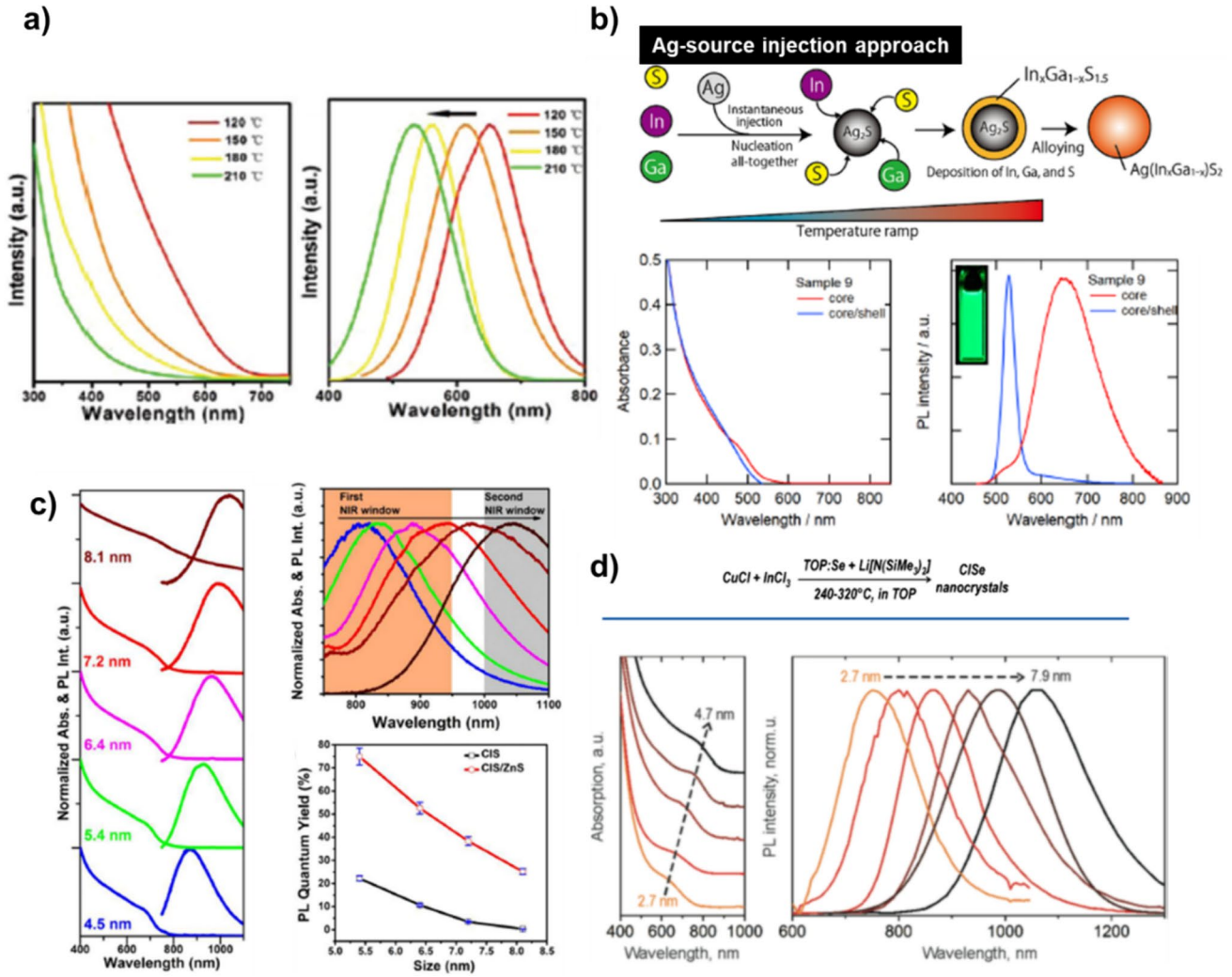

Fig. 3 **a** Absorption/PL spectra of AIS QDs at different diffusion temperatures. Reproduced with permission [42]. Copyright 2012 American Chemical Society. **b** Schematic of the synthesis of AIGS QDs using Ag source injection approach and absorption/PL spectra of as-prepared AIGS and AIGS/ZnS QDs. Reproduced with permission [48]. Copyright 2023 American Chemical Society. **c** Absorption/PL spectra of CIS QDs prepared by cation exchange using different sizes (4.5 – 8.1 nm) of template $Cu_{2-x}S$ QDs and PL spectra of CIS/ZnS QDs using different sizes (4.5 – 8.1 nm) of CIS QDs, with their PLQYs. Reproduced with permission [51]. Copyright 2017 American Chemical Society. **d** Reaction pathway toward CISe QDs and absorption/PL spectra of different size CISe QDs. Reproduced with permission [54]. Copyright 2013 American Chemical Society

In/Ga/S precursors. The As-synthesized AIGS QDs were coated with GaS_y shells using $Ga(OAc)_3$, $Ga(DDTC)_3$, and dimethylthiourea in OAm. After coating with GaS_y shells, the core/shell QDs exhibited intense band-edge emission between 499 and 543 nm with a narrow FWHM of 31 nm and a PL QY above 50%.

$CuInS_2$

As representative I–III–VI QDs, $CuInS_2$ (CIS) QDs are direct band-gap semiconductors with a bulk bandgap of only 1.45–1.53 eV. The exciton Bohr radius of CIS is 4.1 nm, and quantum-confinement effects can be observed in CIS QDs when their size is reduced to 8 nm. Their optical bandgaps can be controlled by their size and composition, resulting in emission wavelengths ranging from visible to NIR. Also. CIS QDs have large absorption coefficients (~ 10^5 M^{-1} cm^{-1} at the first excitonic transition) and low toxicity, making them suitable for optoelectronic devices and biological applications. In general, the emission wavelength can be easily tuned to the NIR by increasing the [Cu]/[In] ratio during the synthesis of CIS QDs. Ternary CIS QDs possess off-stoichiometry and can tolerate a larger stoichiometric ratio deviation while keeping the crystal shape unchanged, thus forming a high density of defect-state energy levels. The wide distribution of the defect-state energy levels in

the midgap resulted in broad FWHM characteristics of the PL spectra of the CIS QDs. CIS has three crystal types: chalcopyrite (CP), zinc blende (ZB), and wurtzite (WZ). According to previous reports, stable CP crystals tend to form at low temperatures (~ 150 °C), while metastable ZB and WZ crystals tend to form at high temperatures (~ 230 °C). Many studies have shown that the geometry and crystal shape of CIS QDs are affected by reaction temperature, precursor reactivity, ligand type, and reaction solvent. In the past, the synthesis of CIS QDs with CP structures underwent a transformation from a single-source precursor such as $(PPh_3)_2CuIn(SEt)_4$ to a multi-precursor, considerably simplifying the experimental process and reducing costs [49]. However, the multi-precursor synthesis of CIS QDs requires the reactivity of three different precursors (Cu, In, and S) to achieve a strict balance that prevents the formation of binary byproducts (Cu_2S and In_2S_3) or other heterogeneous nanoparticles, such as Cu_2S–CIS. Klimov et al. synthesized single-crystalline sub-10 nm CIS QDs by a heating method using copper iodide and indium acetate dissolved in DDT and OA as controlled precursors [50]. The As-synthesized CIS QDs had a CP phase, resulting in a stoichiometry close to 1:1:2 and a tunable size with reaction time. In this reaction, DDT and OA were used as the stabilizing ligands for Cu^+ and In^{3+}, respectively, and provided proper control of the precursor reactivity, resulting in homogeneous CIS QDs with a CP structure. Furthermore, epitaxial growth to form a ZnS shell on the as-synthesized CIS QDs resulted in a maximum PLQY of approximately 70% in the PL range of 630–780 nm. Interestingly, the CIS QDs obtained by CE adopted a metastable WZ structure instead of the CP structure typically observed for CIS QDs synthesized by direct routes (Fig. 3c) [51], thus creating new opportunities to expand the spectral tunability of CIS QDs, as WZ CIS QDs emit at lower energies than their CP counterparts. CIS QDs in the metastable wurtzite phase have been synthesized and generally involve TOPO, which serves as a co-complexing ligand. During the initial stages of these reactions, binary hexagonal $Cu_{2-x}S$ nanocrystals are formed and subsequently transformed into ternary hexagonal CIS QDs via cation exchange with the In-TOP complex. The CIS QDs were then coated with ZnS shells using $Zn(st)_2$ and TOP-S, resulting in WZ CIS/ZnS core/shell QDs with tunable PL from 750 to 1100 nm and PLQYs of up to 75% at 820 nm.

$CuInSe_2$

$CuInSe_2$ (CISe) has a small bulk bandgap of 1.04 eV, a relatively large exciton Bohr radius of ~ 10.6 nm, and a high absorption coefficient (~ 10^5 cm^{-1}). In particular, the CISe QDs in the strong quantum-confinement regime were predicted to be PL emitters in the red and NIR regions. Consequently, the synthesis of CISe QDs has been extensively studied to improve their PL properties. Bawendi et al. reported CISe QDs with PL emission from 690 to 975 nm using bis(trimethylsilyl selenide) precursor at 280–360 °C [52]. Dubertret et al. further refined the reaction to prepare an emissive CISe/ZnS core/shell using selenourea as the selenium precursor and zinc-bis(ethylxanthogenate) as the ZnS precursor [53]. The prepared CISe/ZnS QDs exhibited emission maxima ranging from 700 to 1030 nm with a PLQY of ~ 10–50%. A lattice mismatch between the core and shell materials can prevent the passivation of the surface traps, hindering bright PL. The ZnSe shell can provide higher efficiencies than the ZnS shell, because ZnSe has a relatively small lattice mismatch of 2% with CISe, whereas the lattice mismatch for CISe/ZnS is ~ 7%. Wood et al. reported CISe/ZnSe core/shell QDs with a PLQY 60% higher than that of 50% CISe/ZnS QDs (Fig. 3d) [54]. The growth of ternary copper-based compounds on CISe NCs may provide an opportunity to further improve the PLQY because of the similar metal elements in the core and shell. Rogach et al. introduced a direct synthetic approach for depositing ternary CIS shells on a CISe core using the decomposition reaction of DDT, and the PLQY of the CISe/CIS core/shell QDs improved to 4.5% from the initial value of 0.4% for the CISe core [55]. Different multinary copper-based shells, such as $CuInZnS_2$ (CIZS), $CuInS_{2-x}Se_x$(CISSe), and $CuInZnS_{2-x}Se_x$(CIZSSe), were fabricated by cation-exchange reaction through additional injection of selenium in OAm and zinc oleate during the growth of a CIS shell. The highest PLQY of 20% was achieved for the CISe/CIZSSe core/shell QDs, somewhat lower than that of CISe/ZnSe.

Zinc Chalcogenides

ZnS

ZnS has a large bandgap of 3.72 eV and 3.77 eV [for cubic zinc blende (ZB) and hexagonal wurtzite (WZ) ZnS, respectively], and its wide bandgap provides a barrier layer that passivates surface traps and confines the excitons to the core materials, thereby increasing the PLQY. ZnS is also a common host for luminescent dopants (e.g., Co^{2+}, Cu^{2+}, Pb^{2+}, and Mn^{2+}) with a variety of luminescent properties when excited by UV, X-rays, cathode rays, and electroluminescence (EL). Owing to its excellent transmission property and high refractive index (2.27 at 1 μm), ZnS is also a very attractive candidate for applications in novel photonic crystal devices operating in the visible to NIR range. In 2003, Hyeon and co-workers proposed a general synthetic procedure for the formation of zinc-blende ZnS QDs [56]. In this synthesis, the Zn precursor was prepared in situ by dissolving the $ZnCl_2$ in OAm and TOPO, and then, elemental sulfur

dissolved in OAm was added at room temperature and the reaction was initiated by heating to 340 °C. Uniform spherical ZnS NCs with an average diameter of 8.2 nm exhibited an excitonic peak at approximately 310 nm and PL peaks at 342 and 450 nm, attributed to band-edge and trap state emissions. Zhao and co-workers synthesized hexagonal ZnS QDs at temperatures as low as 150 °C using $ZnCl_2$ and S as precursors in ethylene glycol [57]. The As-synthesized ZnS QDs had an average size of less than 5 nm with absorption peaks (< 325 nm), but no PL properties were observed. Peng et al. developed another approach for growing ZnS QDs using zinc alkyl carboxylate precursors [58]. In this synthesis, ODE-Se was injected into $Zn(st)_2$ in tetracosane and ODE at 340 °C, and the reaction solution was reacted at 300 ℃. The as-synthesized ZnS QDs exhibit an absorption peak at 300 nm and PL peaks at 320 and 400 nm. Recently, Owen et al. reported a method for synthesizing ZnS QDs using zinc carboxylate and thiourea derivatives (Fig. 4a) [59]. They controlled the reactivity of thiourea derivatives by modifying the thiourea structure (N,N′-disubstituted or N,N,' N′-trisubstituted thiourea). The resulting ZnS QDs had a size of 1.7–10 nm with a narrow size distribution and distinct absorption features.

ZnSe

Bulk ZnSe with an energy bandgap of 2.7 eV, which has natural superiority in the blue emission region, has been identified as the most promising heavy-metal-free blue emitter. The ZnSe QDs exhibited a near-unity PLQY

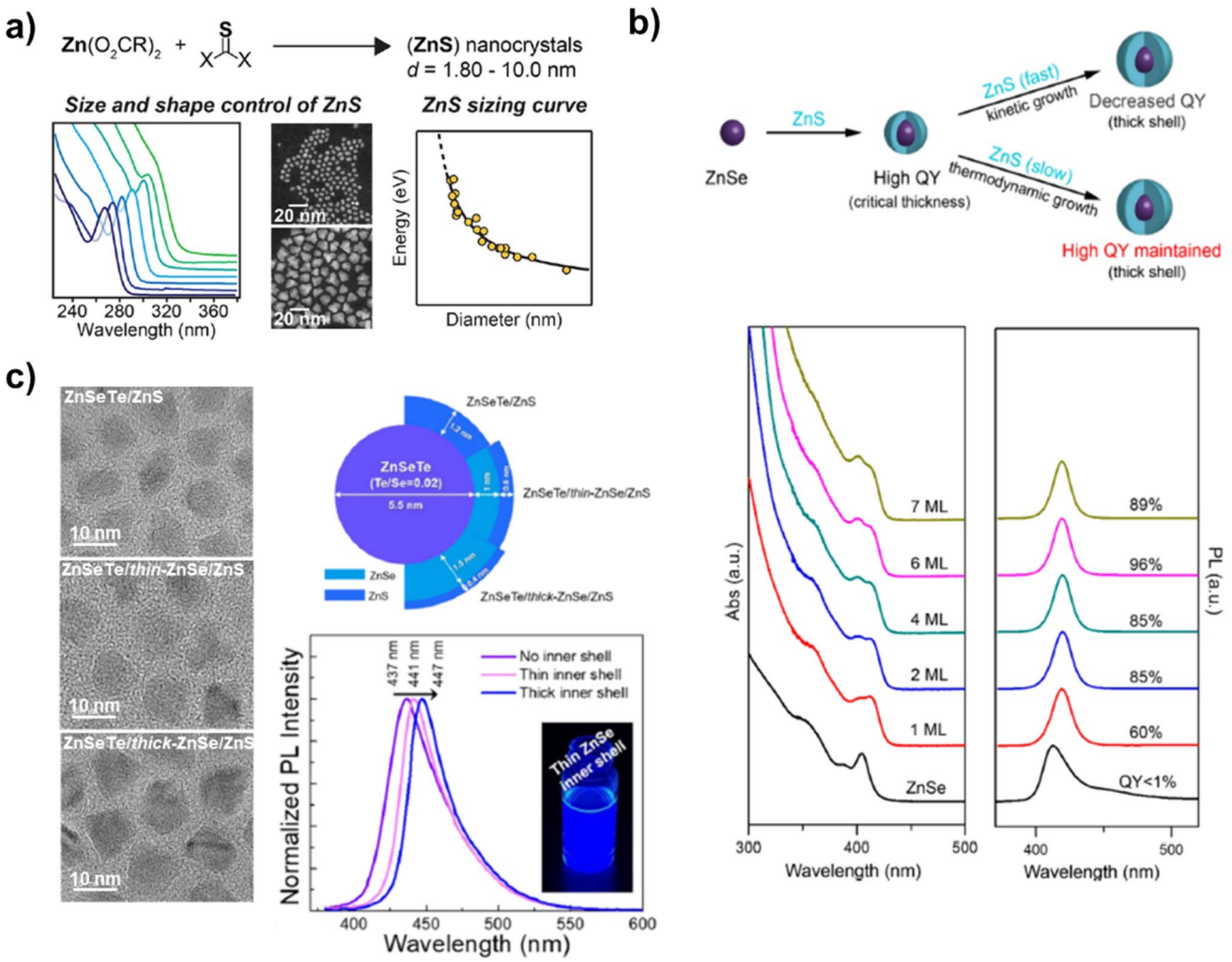

Fig. 4 **a** Reaction scheme for the synthesis of ZnS QDs from zinc carboxylates and substituted thiourea, and their size-dependent absorption spectra and HAADF-STEM images, along with energy of transition vs. diameter determined by STEM. Adapted from [59]. Copyright 2022 American Chemical Society. **b** Schematic illustration of the controlled shell growth of ZnS on ZnSe QD, and absorption/PL spectra of as-prepared ZnSe and ZnSe/ZnS QDs. Reproduced with permission [62]. Copyright 2020 American Chemical Society. **c** TEM images of ZnSeTe/ZnSe/ZnS QDs with different shell structures, with their PL spectra. Reproduced with permission [65]. Copyright 2017 American Chemical Society

and narrow FWHM, but the emission peak was mainly concentrated in the high-energy blue-violet regions (< 450 nm). Research on ZnSe QDs dates back to the year 1998. Guyot-Sionnest et al. synthesized monodisperse and highly luminescent zinc-blende ZnSe QDs in a hexadecylamine (HAD)/TOP coordination solvent [60]. They used Et_2Zn and TOP-Se as Zn and Se sources, and then rapidly injected them into the solvent at 270 ℃. Depending on the reaction time, the as-synthesized ZnSe QDs exhibited a size-tunable PL between 365 and 443 nm, with a PLQY of 20–50%. However, the choice of coordinating solvent makes it difficult to control nucleation and growth, resulting in relatively sluggish growth compared to that of Cd-based QDs. Therefore, non-coordinating solvent–ligand combinations that are more selective and effective in controlling QDs have been developed. Peng et al. synthesized monodisperse ZnSe QDs by reacting $Zn(st)_2$ and TBP-Se in non-coordinating ODE solvent and ODAm ligand at 330 ℃ [58]. The synthesized ZnSe QDs exhibited a PLQY as high as 50% with an FWHM as narrow as 14 nm. To further improve the PLQY of ZnSe QDs, Banin et al. reported ZnSe/ZnS core/shell QDs with a high PLQY [61]. They used $Zn(OA)_2$ and elemental Se powder dispersed in TOP as the precursors for ZnSe QDs. Depending on the reaction time and additional precursors, the size of QDs was controlled from 4.0 to 5.4 nm under an emission range of 412–440 nm. ZnSe QDs were coated with a ZnS shell using Zn oleate and OT was injected using the successive ionic layer adsorption and reaction (SILAR) technique. The as-synthesized ZnSe/ZnS QDs had a size of 8–10 nm and a PLQY of 40%–89% at 420–440 nm. Owing to the large bandgap of ZnSe, the size of ZnSe QDs should be significantly larger to reach the blue color range for display applications. Recently, following the LaMer model, Zhong et al. developed large homogeneous ZnSe/ZnS core/shell QDs by controlling the injection sequence of Zn and Se precursors with high or low reactivity using a seed-mediated strategy (Fig. 4b) [62]. They used diphenylphosphine (DPP)-Se/Zn-OA-OAm (OA:OAm = 0.2) as the high-reactivity precursor and ODE-Se/Zn-OA-OAm (OA:OAm = 1) as the low-reactivity precursor. The resulting ZnSe core achieved pure blue emission between 455 and 470 nm with an average particle size of 8–35 nm. For the ZnS shell, the authors used $Zn(OAc)_2$ and OT, TOP-S at 300 ℃. The synthesized ZnSe/ZnS QDs exhibit a maximum PLQY of 60% at 455 nm.

ZnSeTe

The most feasible means of obtaining deep blue PL from ZnSe QDs is to form ternary ZnSeTe QDs by alloying with ZnTe, which has a smaller bandgap (2.25 eV). The synthesis of blue-emitting ZnSe QDs was previously demonstrated using aqueous colloidal methods [63]. Zn precursor solutions were prepared by mixing $Zn(ClO_4)_2$-$6H_2O$ and TGA, and the solutions were adjusted to pH 6.5. A mixed gas of H_2Se and H_2Te was passed through and the resulting solution was reacted at 100 ℃ for 48–72 h. However, their blue PL properties were quite poor (< 30% in QY and > 75 nm in FWHM) mainly due to less-advanced synthetic chemistry and core/shell heterostructure. Recently, Yang et al. reported the viable synthesis of blue ZnSeTe/ZnSe/ZnS core/shell QDs with PL wavelengths of 437–447 nm, QYs of 52–72%, and FWHMs of 30–40 nm, depending on the inner ZnSe shell thickness [64]. The ZnSe core was prepared by reacting $Zn(st)_2$ and Se in ODE with TOP-Te at 300 °C. For ZnSe/ZnS shell coating, Zn oleate, TOP-Se, TOP-S, and OT were used as precursors and reacted at 280 °C. The same group reported a synthesis method using Se-diphenylphosphine (Se-DPP) to promote Se reactivity, thereby achieving a reaction balance between Se-DPP and Te-TOP (Fig. 4c) [65]. The As-synthesized ZnTeSe QDs with triple-shell ZnSe/ZnSeS/ZnS exhibited tunable PL wavelengths of 495–532 nm along a high PL QY of 68–83%, depending on the Te/Se feed molar ratio used for the core synthesis. Jang et al. synthesized ZnSeTe/ZnSe/ZnS QDs using HF and $ZnCl_2$, which etched the surface oxidized states and provided additional Cl^- passivation, resulting in a PL QY of ~ 100% [66]. We summarize the synthesis methods and PL properties of representative non-toxic QDs in Table 1.

Advanced Display Application of Non-toxic QD

Non-toxic QDs can be used in two main fields. One is in optoelectronic devices, particularly in display applications, and the other is in bio-applications.

In particular, when examining applications in the display field, QDs, which are inorganic materials, exhibit superior stability compared to organic materials used in organic light-emitting diodes (OLEDs), making them highly sought-after next-generation luminescent materials. QDs are used primarily in TVs and monitors. In particular, Samsung Electronics has commercialized products integrating QD enhancement films (QDEF) into LCDs and QD-OLED displays by employing QD color-conversion technology in OLEDs by Samsung display. Furthermore, companies, such as TCL and BOE in China, UbiQDs in the United States, and Nanoco in the United Kingdom, are actively developing displays that incorporate QDs. Recently, research on the use of QDs as color-conversion layers in microLEDs for high-resolution displays has been actively pursued.

QDs are gaining attention in the display industry because of their narrow bandwidth, which enables them to provide high color purity for red (R), green (G), and blue (B), thus allowing for a wide range of color representations.

Table 1 Representative overview of the solution-phase synthesis methods for non-toxic QDs

Composition	Method	Precursor	Core size	Shell precursor	Core/shell size	PL wavelength	Max. QY	References
InP/ZnSe/ZnS	Hot injection	TOP-P(TMS)$_3$ In(OAc)$_3$	3.3 nm	Zn(OAc)$_2$ TOP-Se TOP-S	11 nm	630 nm	100%	[14]
InN	Hot injection	TMIn, $NaNH_2$	5–15 nm	–	–	500–750 nm	–	[21]
InGaP/ZnSeS/ZnS	Cation exchange	GaI_3 InP core	–	$ZnCl_2$ TOP-Se TOP-S	5.4–5.7 nm	465 nm	80%	[25]
Ag_2S	Dropwise	AgOAc Na_2S	2.1–4.5 nm	–	–	1220 nm	38.6%	[30]
Ag_2Se/ZnSe	Hot injection	AgTFA TOP-Se	2.0 nm	Zn(OAc)$_2$	2.2 nm	1030 nm	40%	[36]
AgAuSe	Cation exchange	$HAuCl_4$ Ag_2Se core	4.5 nm	–	–	970 nm	87.2%	[38]
$AgInS_2$/ZnS	Heating up	AgOAc In(OAc)$_3$	4.2 nm	Zn(OAc)$_2$ Thiourea	5.4 nm	700 nm	> 64%	[43]
$AgInGaS_2/GaS_x$	Heating up	$InCl_3$ In(DDTC)$_3$ Ga(DDTC)$_3$ AgOAc	4.1 nm	Ga(acac)$_3$ Ga(DDTC)$_3$ Dimethylthiourea	4.5 nm	543 nm	75%	[48]
$CuInS_2$/ZnS	Cation exchange	In$(NO_3)_3$-TOP $Cu_{2-x}S$ core	4.5–8.1 nm	Zn(st)$_2$ TOP-S	7.4 nm	820–1050 nm	75%	[51]
$CuInSe_2$/ZnSe	Hot injection	CuCl $InCl_3$ TOP-Se LiN$(SiMe_3)_2$	3.7 nm	TOP-Se $ZnEt_2$	4.2 nm	800 nm	60%	[54]
ZnS	Hot injection	Zn oleate N,N-alkyl thiolurea	1.8–10 nm	–	–	–	–	[59]
ZnSe/ZnS	Hot injection	Se-DPP Zn(OAc)$_2$	8.8 nm	Zn(OAc)$_2$ OT TOP-S	11.8 nm	455 nm	60%	[62]
ZnSeTe/ZnSe/ZnS	Hot injection	$ZnEt_2$ TOP-Se TOP-Te	3.1 nm	Zn(OAc)$_2$ TOP-Se TOP-S	10.8 nm	457 nm	100%	[66]

Therefore, QD displays can reproduce colors that are very close to what the human eye perceives, thereby enhancing the viewing experience. In the realm of displays, the term "color space" refers to the specifications governing color representation. These standards vary among institutions and companies. CIE 1931, introduced by the International Commission on Illumination (CIE) in 1931, remains the most widely used traditional standard. The rainbow diagram shows the visible spectrum perceived by the human eye. The term "color gamut" quantifies the extent to which the colors depicted in the original can be represented on a screen, indicating the range of colors that can be displayed. Commonly used standards in the color space include sRGB, Adobe RGB, and NTSC. The sRGB, created in 1996 by HP/MS, is a standard color space. Adobe RGB, established by Adobe in 1998, aims to improve the green and cyan color loss in sRGB. NTSC, designated by the International Telecommunications Union, is a space used for international television broadcasting standards. Another widely used standard in recent high-color-gamut displays is BT.2020. Here, BT.2020, also known as Rec.2020, denotes the color space standard for broadcast video established by the International Telecommunication Union (ITU), formally known as "ITU-R Recommendation BT.2020," commonly abbreviated as "Rec.2020" or "BT.2020." The "BT" in BT.2020 stands for Broadcasting service (television), and BT.2020 represents the current predominant UHDTV color space (Fig. 5a) [67]. QDs are known that QDs serve as high-color-gamut materials capable of satisfying over 90% of the BT.2020 standard. As shown in Fig. 5b, we observed variations in the area occupied by the color space depending on the bandwidths of the r, g, and b spectra [68]. Therefore, using QDs makes it possible to emit red, green, and blue with much narrower bandwidths than the emission bandwidth of organic materials in OLEDs, thus enabling the representation of a wider range of colors.

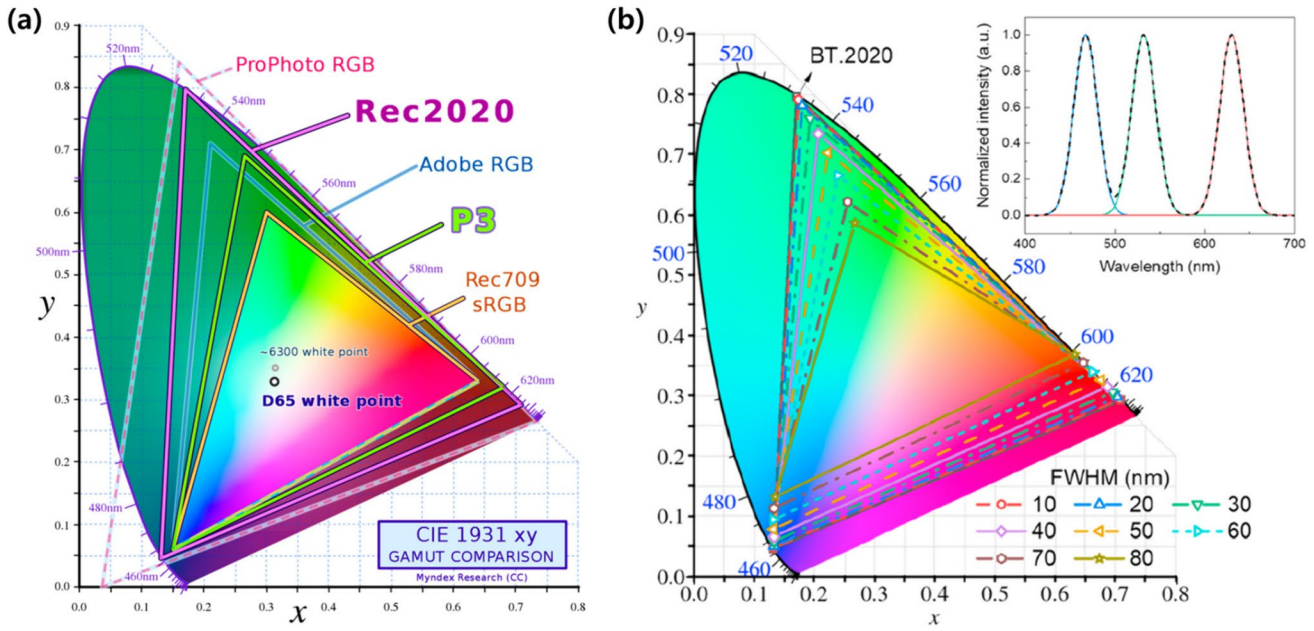

Fig. 5 **a** CIE 1931 chromaticity diagram illustrating the color gamuts of standards, such as sRGB, DCI-P3, Rec2020, AdobeRGB, and ProPhoto. Reproduced with permission [67]. Copyright 2023 Multidisciplinary Digital Publishing Institute. **b** CIE (x, y) chromaticity coordinates depict the white spectrum composed of blue, green, and red primary colors, each with varying full-width at half maximum (FWHM) values of PL spectra. The inset shows the white spectrum with a consistent 30-nm FWHM across all primary colors. Reproduced with permission [68]. Copyright 2020 Elsevier

In the field of displays, technology is distinguished based on whether QDs are used as color-conversion layers (utilizing the PL characteristics of QDs) or emitting layers (utilizing the EL characteristics of QDs). All the currently developed and commercialized QD displays utilize the PL method (Fig. 6). EL methods are still in the research stage and face numerous challenges that need to be addressed before they can be commercialized [69, 70].

Displays represent the visible-light spectrum of our eyes. Therefore, display technologies based on non-toxic QDs have been developed using QDs that emit light in the visible-light spectrum. Initially, color-conversion and EL displays were primarily developed using Cd-based QDs. However, in 2006, the enforcement of the restriction of hazardous substances directive (RoHS) by the European Union prohibited the sale of products containing more than

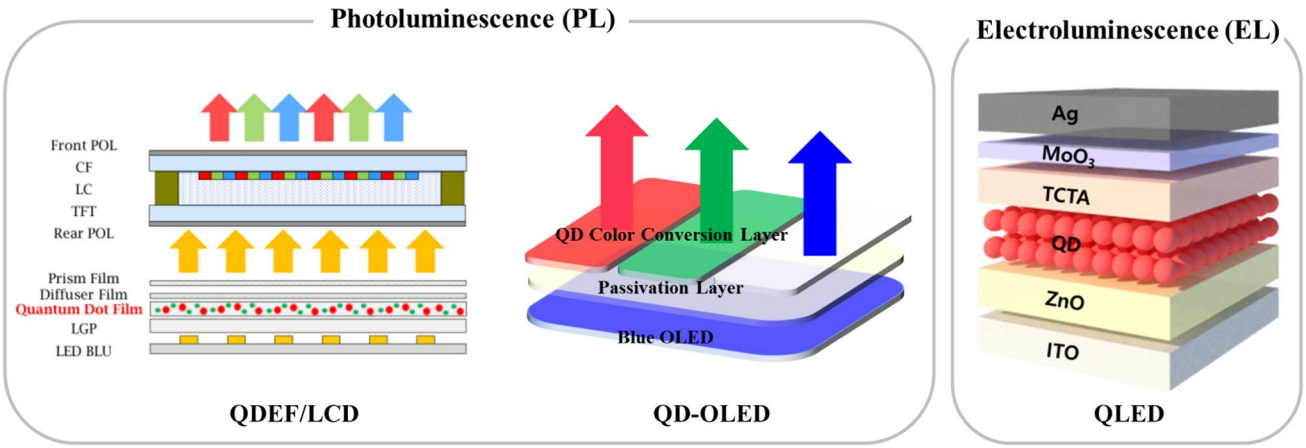

Fig. 6 Schematic diagram depicting QD enhancement film (QDEF). Reproduced with permission [69]. Copyright 2018 SID Symposium Digest of Technical Papers utilizing PL emission, QD-OLED employing QD color conversion, and QLED operating under EL. Reproduced with permission [70]. Copyright 2019 Royal Society of Chemistry

0.01 wt% of cadmium. Consequently, the development of environmentally friendly QD materials free from heavy metals has gained momentum. The QDs introduced in this review, such as those belonging to the III–V group, II–VI group, and I–III–VI groups, are being developed. Materials based on III–V group semiconductors, such as InP QDs, are utilized for displays, because InP materials have bandgaps within the visible-light spectrum, making them suitable for display applications. All QDs used in the QD-enhanced displays found in current commercialized TVs are based on InP QDs. Both QD enhancement film (QDEF) and QD color-conversion layers utilize different light sources for blue light (e.g., LCD, blue OLED, or blue LED), explaining the reason why green and red QDs are employed, excluding blue QDs.

To date, color-converting QDs have predominantly been based on InP. Research has focused on synthesizing InP-core QDs with ZnS or ZnSe single, multi-, or gradient shells to achieve high absorbance, luminescence efficiency, and stability. Regarding the red color, the InP-based QDs exhibited sufficient absorption and emission characteristics with blue light sources [14, 71]. However, for green, the blue absorption of InP QDs is too low, which limits their application as color-converting materials. Further research is underway to improve on this aspect. For instance, studies have involved alloying GaP with InP or synthesizing QDs based on $AgInGaS_2$ rather than InP [24, 72, 73].

QD color-conversion technology initially saw its inception with the application of QDs in LCDs as QDEF, utilizing red and green QDs produced as relatively thick films, nearly at the level of 100 µm. However, recent research has primarily focused on employing QDs as color-conversion layers in OLEDs and microLEDs. Unlike in this case, red and green QDs are utilized separately to construct individual pixels, necessitating a patterning process. There are two main methods for patterning: one involves photolithography to pattern the QD photoresist (PR), and the other involves creating QD ink for inkjet printing (Fig. 7) [74, 75]. The QDPR method is advantageous for semiconductor processes, because it uses the conventional photolithography techniques to pattern QDs. Conversely, research is required to modify the surface of QDs to prevent their aggregation and preserve their optical properties during the formulation process when mixing QDs with PR.

Various QD-CCL technologies exist, and initially, most studies have focused on Cd-based QDs. Although the commercial viability remains uncertain, academic studies continue to explore color conversion using Cd-based QDs, with research findings being published.

NanoSYS developed inks for thermal-curing inkjet printing using InP/ZnS QDs (Fig. 8). The ligands of the QDs were replaced with materials compatible with the ink through ligand substitution methods, allowing the QDs to disperse well in a medium typically used for inkjet printing. The QDs were mixed at high concentrations (15–50 wt.%); as the thickness of the QD color-conversion layer increased, the amount of light passing through the exciting QDs at 450 nm decreased. A transparent ink containing scattering particles to enhance the outcoupling of blue light was applied to the top surface of the blue pixel at the same thickness as the QD ink, because a color-conversion layer was not required for the blue pixel [76].

Although many UV-curable QD inks have been developed along with thermal-curing options, reports have predominantly focused on Cd-based QDs. In addition to inkjet printing, photolithography methods can be used to achieve higher resolution patterns more easily, a process that has been extensively developed by Nanosys [77]. Similar to QD ink, the development of a QD PR is necessary for this process, which requires the modification of the QD surface

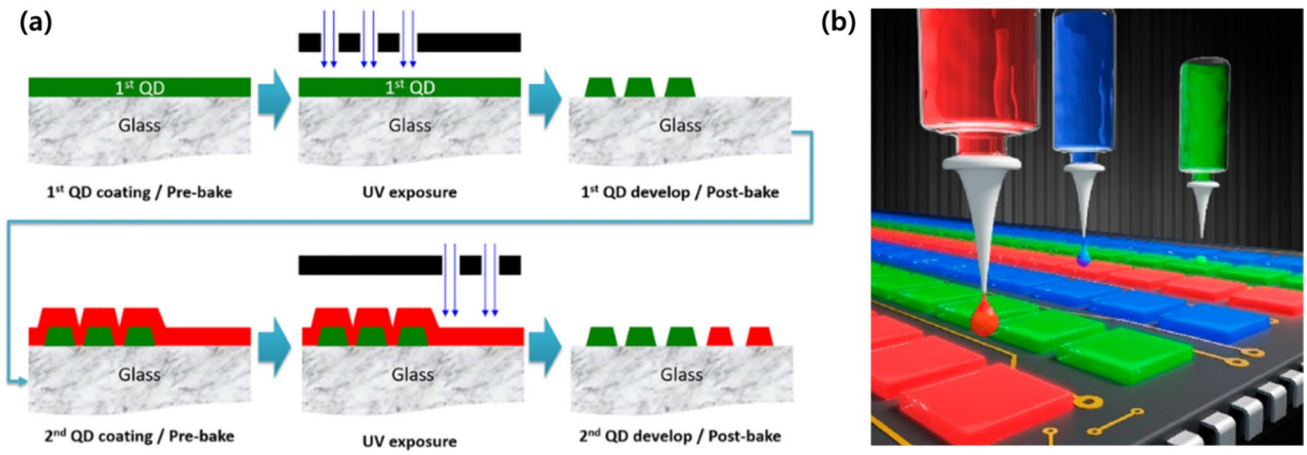

Fig. 7 Schematic diagrams of photolithography method (**a**) and inkjet printing method (**b**) for QD patterning. Reproduced with permission [74]. Copyright 2019 Wiley. Reproduced with permission [75]. Copyright 2020 American Chemical Society

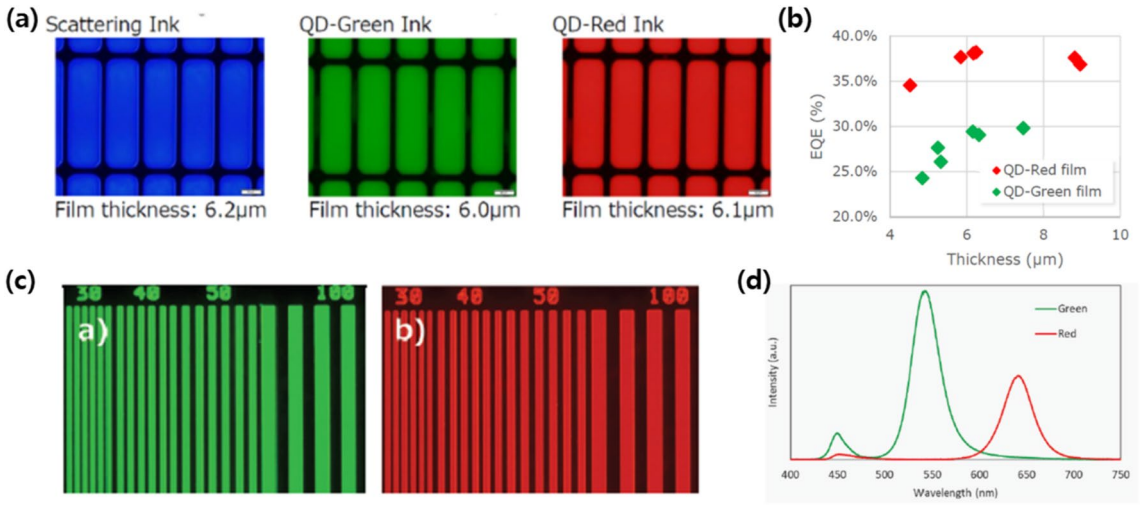

Fig. 8 **a** Optical microscope images of pixel arrays with blue LED backlight. **b** External quantum efficiency (EQE) as a function of QDPR film thickness. Reproduced with permission [76]. Copyright 2018 Wiley. **c** Optical images of green QDPR and red QDPR pattern, and **d** emission spectra of red and green QDPR with a 10 μm thickness. Reproduced with permission [77]. Copyright 2020 Wiley

to ensure compatibility with the PR. It is known that both QD ink and QD PR should have a thickness of approximately 10 μm. Regarding the efficiency of the QD color conversion, as the thickness of the QD-CCL increases, the conversion efficiency also increases. However, excess thickness may cause a decrease in the conversion efficiency owing to reabsorption or FRET between QDs. From the perspective of blue light absorption, thicker QD CCLs absorb more light, which is advantageous. However, considering the efficiency of the QD-CCL, applying an appropriate CCL thickness is more favorable.

EL displays, specifically QD light-emitting diodes (QD-LEDs), replace the emissive layers of conventional OLEDs with QDs. In this structure, electrons and holes injected from both electrodes form excitons in the QD-emissive layer, and light is emitted with energy corresponding to the bandgap of the QDs. QD-LEDs operate based on the same principles as OLEDs with similar structures. Therefore, they may utilize the same electron and hole transport layers as the injection layers developed for OLEDs or they may incorporate inorganic-based electron transport layers tailored for QDs, thus providing the advantage of leveraging existing OLED infrastructure. Furthermore, QD-LEDs inherit one of the advantages of OLEDs: their ability to create flexible and bendable displays. Research on the production of EL devices using QDs has been extensively reported, with QDs gaining attention as next-generation devices that can succeed OLEDs [77, 78]. They offer the advantage of applying almost identical common layers except for the use of QDs instead of organic dyes, as in the case of OLEDs. A distinguishing factor in QLEDs is the use of inorganic nanoparticles, such as ZnO or ZnMgO, primarily as the ETL layer, unlike OLEDs. The hole transport layer (HTL), which serves as the hole-transporting layer, typically utilizes materials such as CBP, TCTA, NPB, TFB, and poly-TPD. Both normal and inverted structures of QLEDs are under development. Non-toxic QD-based QLEDs are continuously being researched, with recent reports showing improvements in the lifespan of up to a million hours in InP-based QLEDs. Figure 9a and 9b shows a paper on InP QLEDs, which presents the structure and high performance of their QLED device [14]. Figure 9c, d from a paper published in 2023 highlights the fabrication of efficient QLEDs using InP-based red and green QDs, as well as the production of emissive devices on flexible substrates, indicating the potential for future use in human-friendly flexible devices [79].

The patterning of QDs in the EL technology is not significantly different from that in QD-CCL. While the purpose of QD-CCL is to disperse QDs in a polymer medium to create thick layers, in QDEL devices, the QDs themselves serve as the emitting layer (EML), requiring extremely thin layers of QDs (typically monolayers). Many QD-LED devices have been fabricated at the unit-device level, often by simply dispersing QDs in an organic solvent and spin-coating them onto a device. As development progresses at the unit-device level, patterning for actual display applications requires r, g, and b patterning. Similar to the QD-CCL technology, r, g, and b patterning can be achieved through inkjet printing or photolithography. The difference lies in the use of a QD solution without a polymer. However, modifying the QD surface ligands or attaching light-responsive molecules to enable photolithography remains necessary in QD-LEDs for QD patterning.

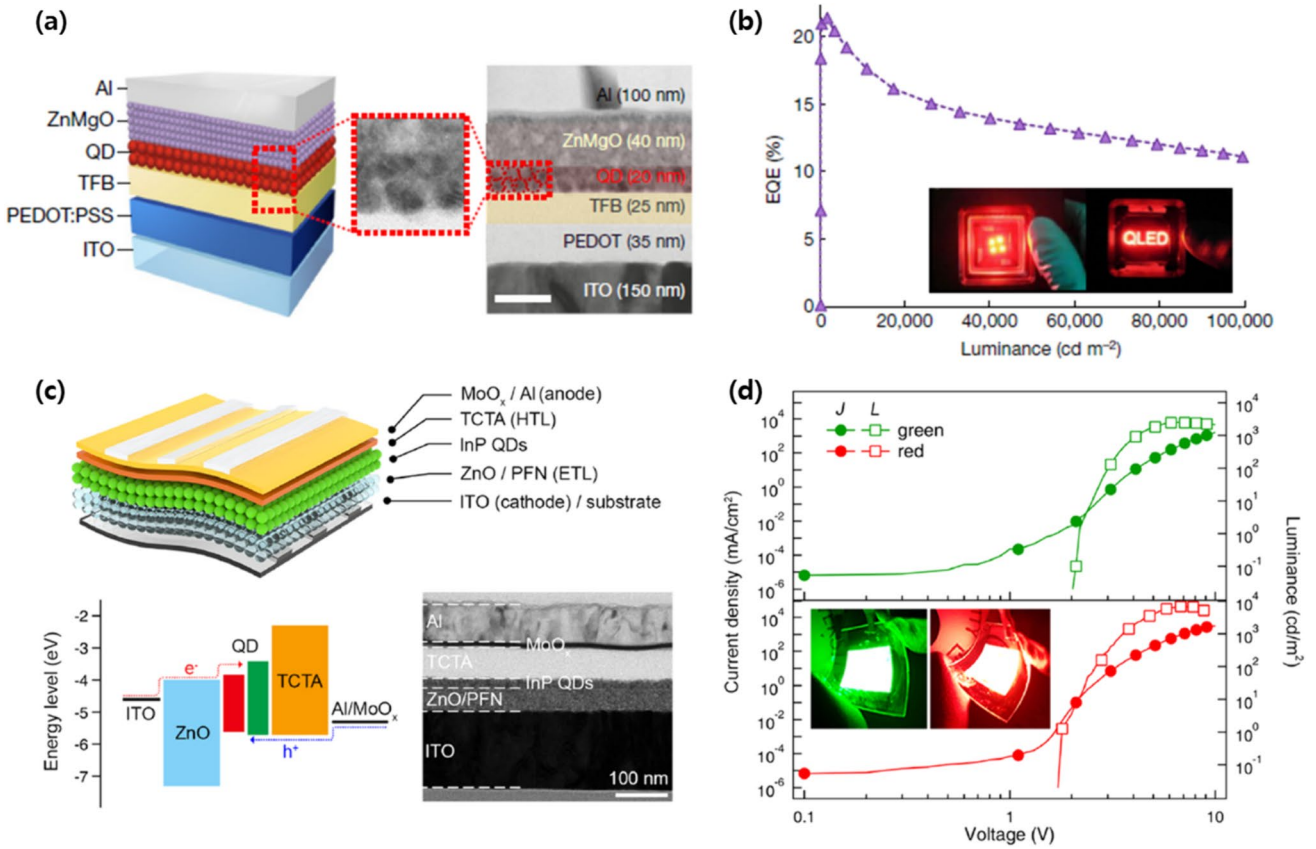

Fig. 9 **a** Illustration and cross-sectional TEM image of InP-based QLED (scale bar: 50 nm). **b** EQE- profile of QLED. Reproduced with permission [14]. Copyright 2019 Nature Portfolio. **c** Schematic illustration, energy band diagram, and cross-sectional TEM image. **d** J–V–L characteristics of flexible red, green InP-QLED. Reproduced with permission [80]. Copyright 2019 American Chemical Society

In QD-CCL technology, the efficiency of the blue component relies on the use of light from OLED or LED sources. Therefore, developing synthesis methods for non-toxic red- and green-emitting QDs with high conversion efficiencies is required. However, in a QDEL where QD self-emission is utilized, QDs emitting red, green, and blue light are required. Table 2 summarizes representative papers on non-toxic QD-based QLEDs.

Bio-application of Non-toxic QD

I-VI QD

Non-toxic or less-toxic QDs, particularly I-VI QDs such as Ag_2S, Ag_2Se, and Ag_2Te QD, have been studied as promising candidates for bio-applications because of their unique optical properties and biocompatibility [96]. Unlike conventional heavy-metal-based QDs, such as cadmium-based QDs, non-toxic I–VI QDs offer several advantages for biomedical use. For example, Ag_2S QDs are inherently safe for biological systems, addressing concerns related to their cytotoxicity and environmental impact [97]. In addition to their biocompatibility, I–IV QDs exhibit exceptional optical properties including narrow emission spectra and tunable emission wavelengths in the NIR range. These features make them ideal for various imaging techniques including fluorescence, bio-imaging, and deep-tissue imaging. The NIR emission window enables enhanced tissue penetration and reduces background autofluorescence, thereby facilitating clearer imaging in complex biological environments.

Ag_2Te/Ag_2S core/shell QDs were synthesized via a two-step method to improve the QD PLQY in the NIR region [98]. The dangling bonds on the Ag_2S QD surface were successfully reduced by the overgrowth of the Ag_2S shell layer over the Ag_2Te core, thereby enhancing the PLQY. In addition to the enhanced PL intensity, the as-prepared Ag_2Te/Ag_2S QDs exhibited better stability than Ag_2Te QDs. Subsequently, in vivo imaging of the $Ag_2Te@Ag_2S$ QDs was performed. After administration of 1560 nm-emitting $Ag_2Te@Ag_2S$ QDs via tail intravenous injection, the vascular networks of the whole mouse were clearly visualized within a few seconds post-injection using an 808 nm laser

Table 2 Device performance of non-toxic QD-based QLEDs

Color	Composition	Peak wavelength (nm)	Max luminance (cd/m^2)	Max EQE (%)	Max CE (%)	Year	References
Blue	ZnSeTe	453	–	11.5	–	2020	[80]
	ZnSeTe/ZnSe/ZnS	441	1,195	4.2	2.4	2019	[64]
	ZnSeTe/ZnSe /ZnSeS/ZnS	445	2,904	9.5	5.3	2020	[81]
	ZnTeSe/ZnSe/ZnS	457	88,900	20.2	–	2020	[66]
	ZnSe/ZnS	441.5	–	1.5	–	2013	[82]
	ZnSe/ZnS	400–455	–	7.83	–	2015	[83]
	ZnSe/ZnS	445	–	12.2	–	2021	[84]
Green	InP/ZnSeS	532	–	0.0008	–	2011	[85]
	InP/ZnSeS	518	3,900	3.46	10.9	2013	[13]
	InP/ZnSe/ZnS	531	13,900	13.6	–	2019	[86]
	InP/ZnSe/ZnS	545	12,646	16.3	57.5	2021	[87]
	InP/GaP/ZnS	527	2,938	6.3	13.7	2019	[88]
	InP/ZnSeS	539	17,400	3.4	21.6	2019	[89]
	InP/ZnSe/ZnS	533	3,000	4.2	30.1	2021	[90]
Red	InP/ZnSeS/ZnS	607	2,849	2.5	4.2	2016	[91]
	InP/ZnSe/ZnS	618	10,000	12.2	14.7	2019	[92]
	InP/ZnSe/ZnS	607	1,600	6.6	13.6	2018	[93]
	InP/ZnSeS	623	27,800	4.4	8.5	2019	[89]
	InP/ZnSe/ZnS	630	100,000	21.4	–	2019	[14]
	InP/ZnSe/ZnS	630	128,577	18.6	–	2021	[94]
	InP/ZnSe/ZnS	632	23,300	21.8	23.46	2020	[95]

(Fig. 10a). The extremely low autofluorescence, absorption, and scattering of the 1560 nm emission afford a prominently high penetration depth for deep-tissue imaging with high feature fidelity.

Ren et al. introduced a facile one-step synthesis of water-dispersive Ag_2S QD functionalized with d-penicillamine without an intricate anaerobic process or high temperatures [99]; d-penicillamine was selected as the sulfur source and ligand, and microwave heating was used to prepare the aqueous phase. The FL peak of the QDs was adjusted from 675 to 719 nm by varying the heating temperature and growth time. After incubation with the QD dispersion, more than 80% of the cells retained their viability at a QD concentration of 100 g/L.

In a recent study, thioglycolic acid-functionalized Ag_2S QDs were prepared by ligand exchange from dodecylmercaptan using excess thioglycolic acid and dodecylmercaptan [100]. Ag_2S QD fluorescence was observed at approximately 1100 nm. Furthermore, the addition of Zn^{2+} and Cd^{2+} significantly enhanced the fluorescence intensity of the synthesized Ag_2S QDs, attributed to the formation of surface passivation around the Ag_2S cores, facilitated by the reaction of Zn^{2+} or Cd^{2+} with the surface thioglycolic acid. This process restores surface defects and suppresses non-radiative pathways, resulting in increased fluorescence intensity. The authors applied the as-prepared sensors during cell incubation and observed a distinct cellular image in the NIR range (Fig. 10d), demonstrating the practicability and robustness of Ag_2S QDs in biological environments. Additionally, the QDs showed promise for detecting intracellular Zn^{2+} levels, as evidenced by the significantly stronger NIR fluorescence observed in the presence of exogenous Zn^{2+}, indicating that the platform can be utilized to detect intracellular Zn^{2+} levels.

Targeted NIR-II probes based on Ag_2S QD and RGD peptides offer superior tumor-targeting capabilities and NIR-II fluorescence properties, enabling precise intraoperative guidance (Fig. 10e) [101]. Unlike previous probes, the Ag_2S-RGD probe achieved remarkable sensitivity in detecting both vascularized and non-vascularized tumor tissues with high tumor-to-background ratios. Surface modification of Ag_2S QD enhanced the tumor-targeting efficiency, facilitating the detection and elimination of tiny tumor metastatic foci as small as 0.2 mm in diameter. In vivo studies have demonstrated the efficacy of Ag_2S-RGD in accurately localizing and excising peritoneal metastases under NIR-II fluorescence imaging guidance, leading to significantly improved tumor detection rates and surgical outcomes. The probe exhibited excellent biocompatibility and low cytotoxicity, making it a promising candidate for clinical translation in tumor staging, preoperative diagnosis, and intraoperative navigation.

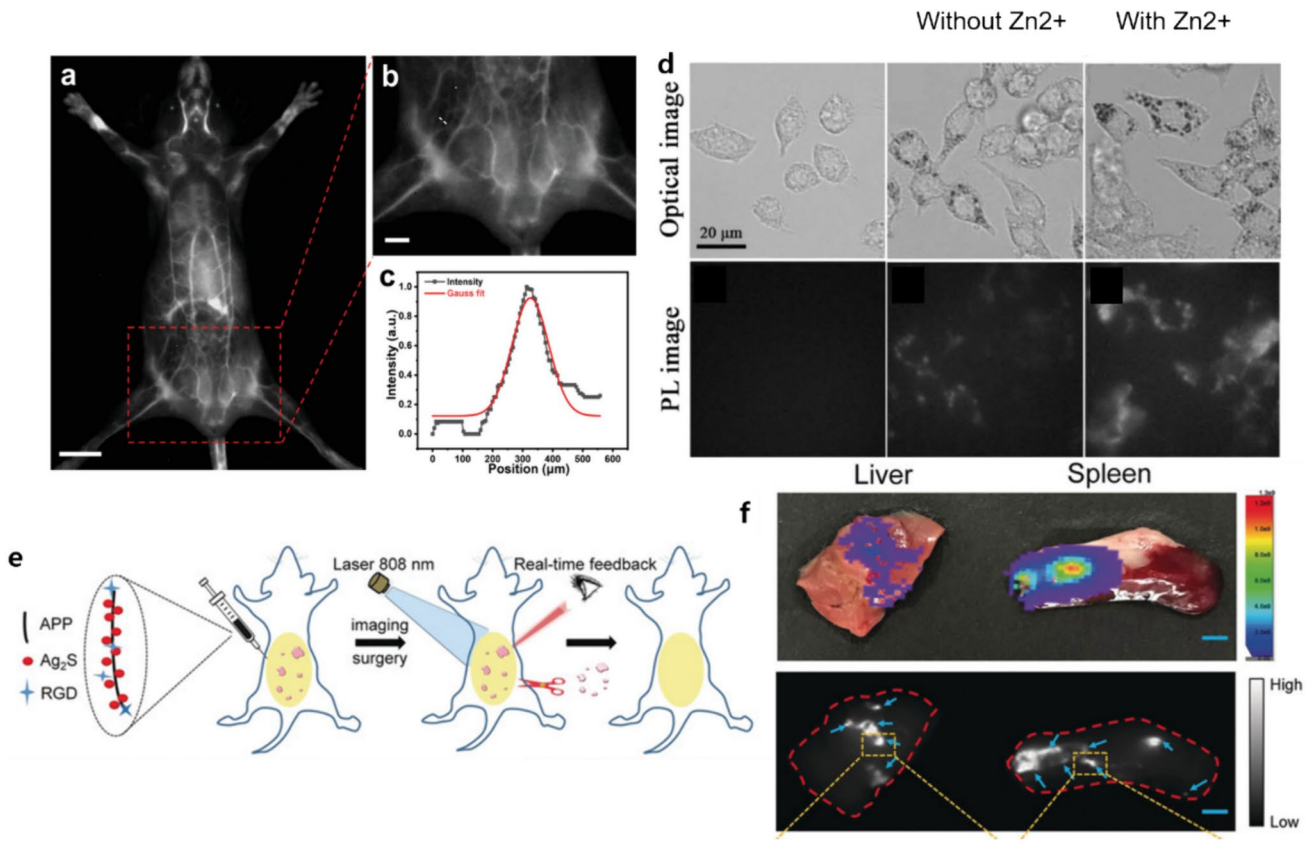

Fig. 10 **a** In vivo fluorescence image of the whole blood vessels of a nude mouse after administration of Ag_2Te/Ag_2s QDs. Scale bar: 3 mm. **b** Magnified fluorescent image of vasculature. Scale bar: 1 mm. **c** A cross-sectional intensity profile measured along the white-dashed line in (**b**). Reproduced with permission [98]. Copyright 2020 Wiley. **d** Optical images of RAW 264.7 cells with the addition of Ag_2S QDs before and after the subsequent mixture of 40 μM Zn^{2+} and their corresponding NIR-II PL images. Reproduced with permission [100]. Copyright 2017 American Chemical Society. **e** Schematic illustration of the NIR-II fluorescent nanochain probe APP-Ag_2S-RGD for image-guided peritoneal carcinomatosis surgery. Bright-field with bioluminescence (RfLuc), and NIR-II images of tumor nodules implanted on several peritoneal organs, including the liver and spleen. Blue arrows indicate metastatic tumor nodules. Scale bar: 1.5 mm. Reproduced with permission [101]. Copyright 2019 Wiley

II–VI QD

In non-toxic II-VI QDs, ZnS, ZnSe, and ZnTe QDs have been increasingly applied in diagnosis and treatment in recent years. Despite their inherent non-toxicity, low PLQY and UV or blue emission make Zn-based QDs difficult to use for bio-applications. Instead, manganese ion (Mn^{2+})-doped II-VI QDs, particularly those utilizing ZnSe or ZnS as hosts, represent a promising solution to the various challenges encountered in the conventional QDs [102]. These Mn^{2+}-doped QDs exhibit strong and characteristic emission, owing to the substitution of Mn^{2+} ions for Zn^{2+} cations within the semiconductor nanocrystal lattice, leading to the $4T_1(4G) \rightarrow 6A_1(6S)$ transition [103]. This emission exhibits significantly higher PL along with excellent thermal, chemical, and photochemical stabilities, attributed to their atomic-like emission states. For example, ZnSe:Mn QDs have been prepared using a phosphine-free nucleation-doping method with zinc stearate, manganese stearate, and selenium powder as the reaction materials [104]. Further peptide functionalization with specific functions enabled the targeting capability to accurately locate obvious or hidden dental lesion sites, thus improving the diagnosis of dental caries. The peptide-functionalized QDs probe was fully dissolved in water and cell culture media and did not show significant harmful effects on human gingival fibroblast cells up to 0.1 g/L concentration. They were able to recognize and adhere to specific *S. mutans* bacteria in comparison with other bacteria (Fig. 11a). These QDs could label the bacterial biofilm on the ex vivo dental caries model, revealing obvious and hidden lesion sites with bright yellow PL.

The Mn-doped ZnSe (ZnSe:Mn) QDs exhibited a remarkably long PL lifetime, similar to that of lanthanide chelates. Considering these properties, time-resolved fluorometry was employed to detect 5-fluorouracil (5-FU), a vital anticancer agent, in human serum [105].

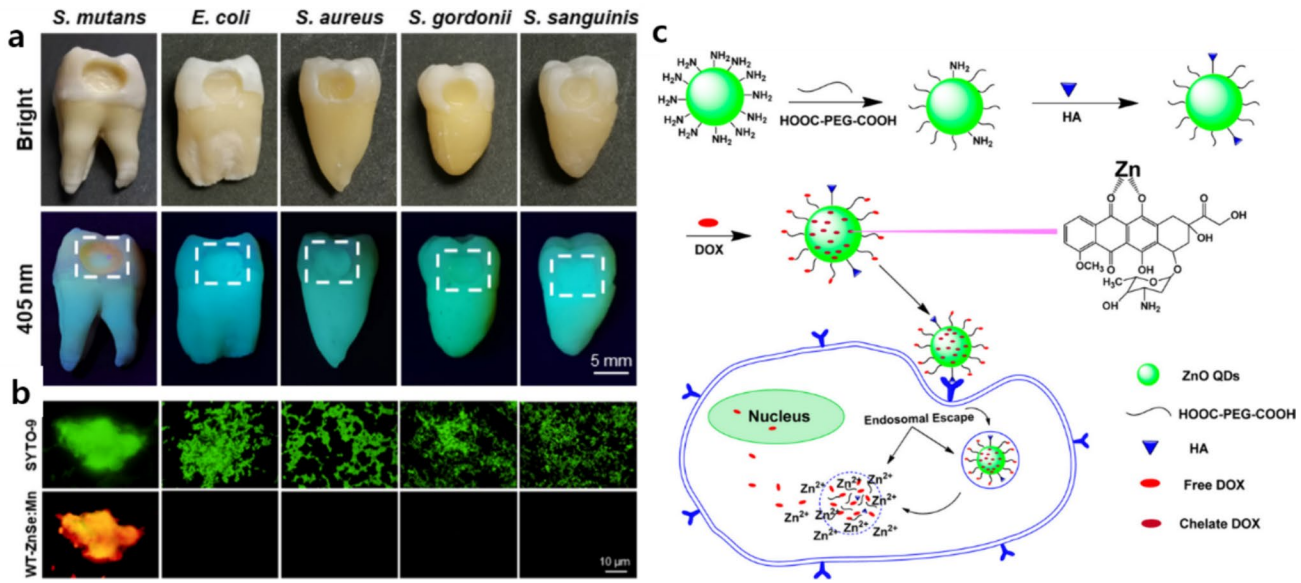

Fig. 11 **a** WT-ZnSe:Mn achieved high-performance imaging in an ex vivo dental caries model. Scale bar, 5 mm. **b** PL images of *S. mutans*, *E. coli*, *S. aureus*, *S. gordonii*, and *S. sanguinis* with WT-ZnSe:Mn and SYTO-9, the orange fluorescence is WT-ZnSe:Mn, and the green fluorescence is SYTO-9. Scale bar: 10 μm. Reproduced with permission [104]. Copyright 2023 American Chemical Society. **c** Assay of working protocol of the hyaluronic acid–ZnO QDs–dicarboxyl-terminated poly(ethylene glycol) (HA–ZnO–PEG) drug delivery system. Reproduced with permission [108]. Copyright 2016 American Chemical Society

Unlike conventional fluorescence methods, time-resolved fluorometry effectively eliminates background noise, enabling the precise detection of targets, such as antigens, proteins, and nucleotides with high sensitivity and dynamic range. Lanthanide chelates are commonly used because of their long fluorescence lifetime, weak luminescence, and susceptibility to photobleaching, which limit their application, especially in real-time biological processes [106]. ZnSe:Mn QDs exhibit superior accuracy by eliminating background fluorescence interference, demonstrating their potential as a new frontier in biomedical sensing [107].

Cai et al. embarked on a pioneering endeavor to develop a drug delivery platform using pH-sensitive ZnO QDs (Fig. 11c) [108]. They synthesized ZnO QDs by loading the anticancer drug doxorubicin (DOX) and investigated the performance of the system in terms of drug release and cytotoxicity. Initially, researchers synthesized water-dispersible, luminescent ZnO QDs and modified their surfaces with amino and poly(ethylene glycol) (PEG) groups to enhance their stability and dispersion. Further modification involved the conjugation of hyaluronic acid (HA) molecules to the ZnO QDs to facilitate targeted delivery to cancer cells expressing CD44 receptors. Next, the anticancer drug DOX was loaded onto HA-modified ZnO QDs. They observed that DOX was rapidly released under acidic intracellular conditions, mimicking the tumor microenvironment. This pH-triggered drug release mechanism was attributed to the dissolution of ZnO QDs and dissociation of the drug–metal complex under acidic conditions. Time-dependent release studies further confirmed the sustained and controlled release of DOX from the HA-modified ZnO QD. Cytotoxicity assays were conducted to assess the antitumor efficacy of HA–ZnO–DOX. They observed a dose-dependent cytotoxicity against A549 lung cancer cells, with HA–ZnO–DOX exhibiting higher antitumor activity than ZnO QDs or DOX alone.

III-V QD

III-V type QDs, such as InP and InGa QDs, are emerging as the luminescent materials of choice because of their intrinsically lower toxicity compared to traditional Cd- and Pb-based QDs [92, 109]. However, high-quality blue-emitting InP QDs have struggled because of the necessity for an ultrasmall QD core (< 2 nm) with reduced defects [109]

Roy et al. synthesized stable blue-emitting InP-based QDs under biological conditions by carefully controlling the growth kinetics of both the core and shell materials [110], achieved by optimizing the precursor amount and growth kinetics, which resulted in highly uniform InP/ZnS QDs with thin ZnS shells. The non-toxic nature of these QDs was demonstrated through cytotoxicity assays, showing > 80% cell viability even at 3 μM QD (Fig. 12a). Cellular bio-imaging studies further validated the suitability

of these QDs as imaging agents with excellent compatibility with other commercially available fluorophores. They highlighted the use of blue-emitting QDs in photo-induced FRET studies. By pairing QDs with rhodamine B dye as the acceptor molecule, researchers have demonstrated efficient energy transfer, paving the way for a wide range of potential applications in biological studies.

Xu et al. synthesized non-toxic InP/GaP/ZnS QD@SiO_2 QD tailored for immunoassay bio-applications [111]. The stability of the hydrophilic QD@SiO_2 was superior to that of its traditional counterparts, InP/GaP/ZnS QD, maintaining PL over a wide pH range and under various stress conditions, such as UV radiation and high temperatures. The synthesized QDs exhibit low cytotoxicity. The QDs were functionalized with CRP antibodies for fluorescence-linked immunosorbent assay (FLISA) (Fig. 12b). Optimization of reaction conditions yielded sensitive detection of CRP, with a limit of detection (LOD) of 0.9 ng/mL, showcasing the potential for high-throughput, sensitive analysis. For biological samples, the QD-based FLISA showed excellent recovery rates, indicating its feasibility in real-world applications. The developed assay exhibited superior sensitivity and a broader

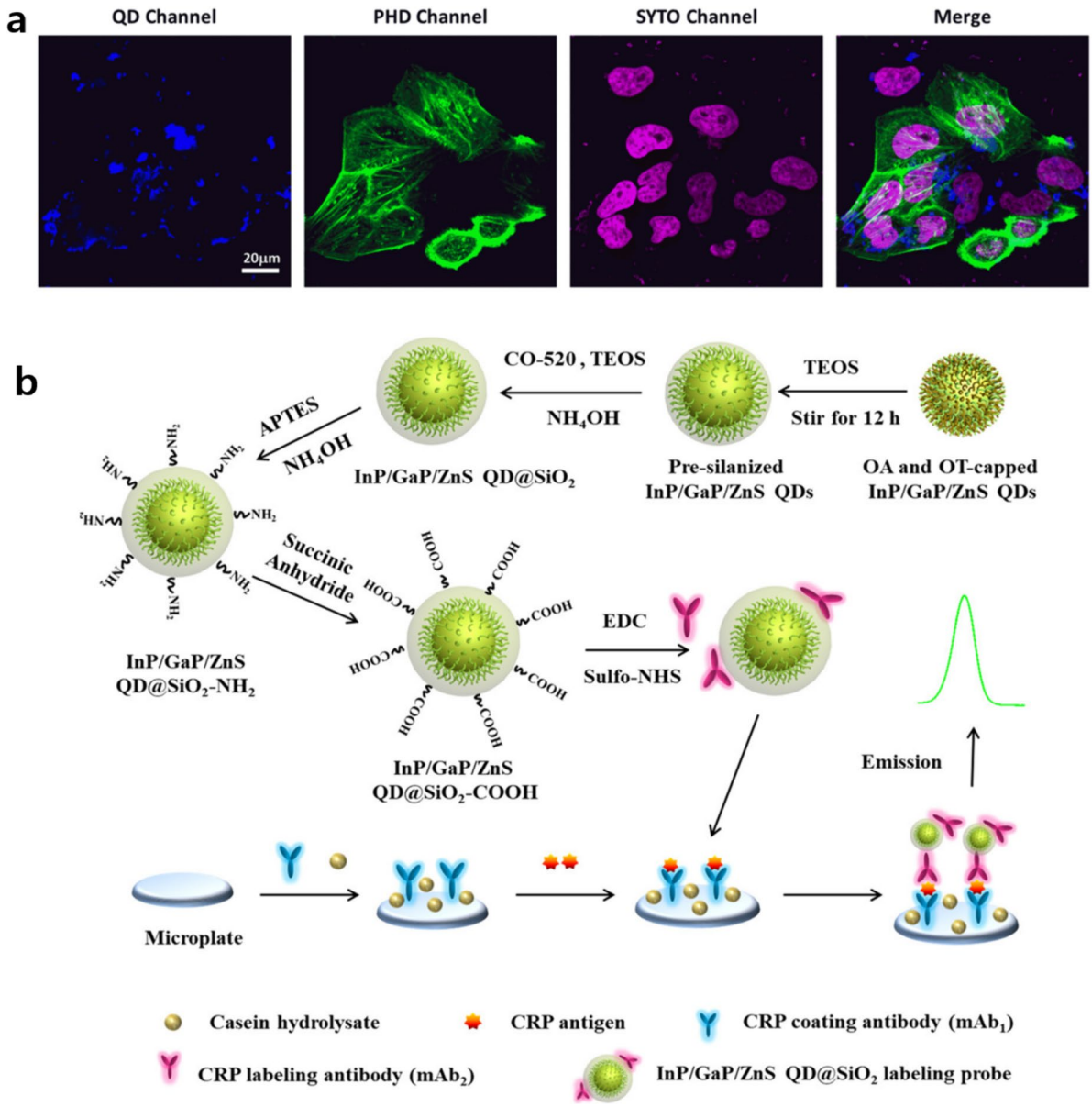

Fig. 12 **a** Multicolor imaging of pure blue-emitting InP/ZnS QDs with PHD and SYTO-Deep Red commercial dyes. Reproduced with permission [110]. Copyright 2023 Royal Society of Chemistry. **b** Schematic of the preparation process of InP/GaP/ZnS QD@SiO_2–COOH nanoparticles and their application in sandwich InP/GaP/ZnS QD@SiO_2–FLISA. Reproduced with permission [111]. Copyright 2021 American Chemical Society

detection range than the existing methods, underscoring its significance in biomedical research.

To explore the in vivo applications of III-V QDs, the biodistribution and fate of non-toxic InP/ZnS QDs were investigated in a mouse model [112]. The surfaces of the QDs were modified with different functional groups (–COOH, $–NH_2$, and–OH) to enhance their biocompatibility. They investigated the biodistribution and acute toxicity of QDs in mice following intratracheal administration. These QDs tend to accumulate in the lungs, especially the -OH-modified QDs; however, the QDs exhibited no major toxic effects, except for transient lung congestion. Further analysis revealed alterations in white blood cell counts, indicating a potential immune response, but no significant abnormalities in the major organs, except for slight lung injury with $-NH_2$ modified QDs. Overall, this study highlights the potential of non-toxic InP/ZnS QDs for biomedical applications, emphasizing the importance of surface modification to enhance biocompatibility. These results suggest that QDs cross the blood–air interface, enter the circulation, and are cleared from the body. Further research in this area is crucial for harnessing the unique properties of QDs while ensuring their safety for use in various biomedical applications.

I–III–VI QD

Non-toxic ternary I–III–VI QDs have also attracted considerable attention as alternatives to toxic QDs [113, 114]. These materials, including AIS, CIS, and AIS/ZnS, exhibit superior control of optical properties by tuning their size and composition CIS, for instance, they emit light in the NIR spectrum with precise energy levels, making them particularly suitable for biomedical applications [115].

Subramaniam et al. showcased the sonochemical synthesis and bio-application of ZnS-coated $Ag_yIn_{1-y}S_2$ (ZAIS) QDs with tunable properties, enabling the simultaneous imaging and delivery of therapeutic RNA molecules to brain tumor cells (Fig. 13a) [116]. The sonochemical synthesis method, which utilizes ultrasound irradiation, offers several advantages including fast reaction rates, controllable conditions, and the formation of uniform nanoparticles with high purity. By varying the precursor concentration, the emission wavelength of ZAIS QDs can be tuned across a wide range, offering unique advantages over traditional QDs. Moreover, the water-soluble ZAIS QDs were stable under physiological conditions without aggregation, exhibiting marginal cytotoxicity even at 0.1 mg/mL concentrations. This biocompatibility was confirmed using cytotoxicity assays in both cancer and stem cells, highlighting its potential for long-term cellular imaging applications. Furthermore, positively charged ZAIS QDs have been successfully used as delivery vehicles for small interfering RNA (siRNAs) in brain tumor cells, resulting in efficient gene knockdown. The ability to track QD-siRNA complexes in real time opens up new possibilities for the targeted delivery and monitoring of therapeutic molecules.

In another study, ZnCuInSe/ZnS core/shell QDs were coated with a multidentate imidazole–zwitterionic block copolymer, resulting in optimized optical properties and long-term stability within the cytoplasm of live cells (Fig. 13b) [117]. They could detect isolated tumor cells circulating in the bloodstream of living rats, achieving velocities in the range of 1 mm/s. Autofluorescent photons from tissues were rejected owing to the efficacy of the time-gated detection. The autofluorescence intensity decreased rapidly with gate delay, with characteristic decay times of 1–5 ns. In contrast, the PL signal from the QD-labeled red blood cells (RBCs) immobilized on a glass coverslip remained even at long gate delays, exhibiting decay times of 100–200 ns, consistent with the measured QD PL kinetics. This study demonstrates the effectiveness of combining long-lifetime NIR QDs with wide-field time-gated fluorescence imaging for the efficient in vivo detection of ex vivo-labeled cancer cells, particularly those circulating freely in the bloodstream.

Chen et al. recently introduced a method for synthesizing high-quality Cu-deficient CISe QDs with a precisely controlled size and exceptional PL (Fig. 13d) [118]. Researchers have investigated the effect of Cu content on the PL of CISe QDs, unraveling the intricate mechanisms governing donor–acceptor pair recombination. Authors developed a "turn-on" nanoprobe for the detection of adenosine triphosphate (ATP), a crucial biomolecule indicative of various diseases. This nanoprobe leveraged the quenching and recovery of the CISe QD PL in the presence of Ce^{3+} ions and ATP, respectively. The Ce^{3+}-conjugated CISe nanoprobe exhibited remarkable sensitivity and selectivity for ATP detection, with a low detection limit of 56 nM. The nanoprobe demonstrated excellent biocompatibility and feasibility for the real-time monitoring of ATP levels in living cells, demonstrating its potential for applications in bio-imaging and biomedical diagnostics.

Conclusion and Perspective

QDs are currently garnering considerable attention owing to their unique optoelectronic properties and low-cost solution processes. Among all the QDs, non-toxic QDs are becoming increasingly important, especially for direct real-world applications. This review presents a summary of the synthetic methods for various non-toxic QDs and their bio- and display applications. Depending on the atoms that make up the QDs, various strategies have been proposed to synthesize high-quality non-toxic QDs, including precursor

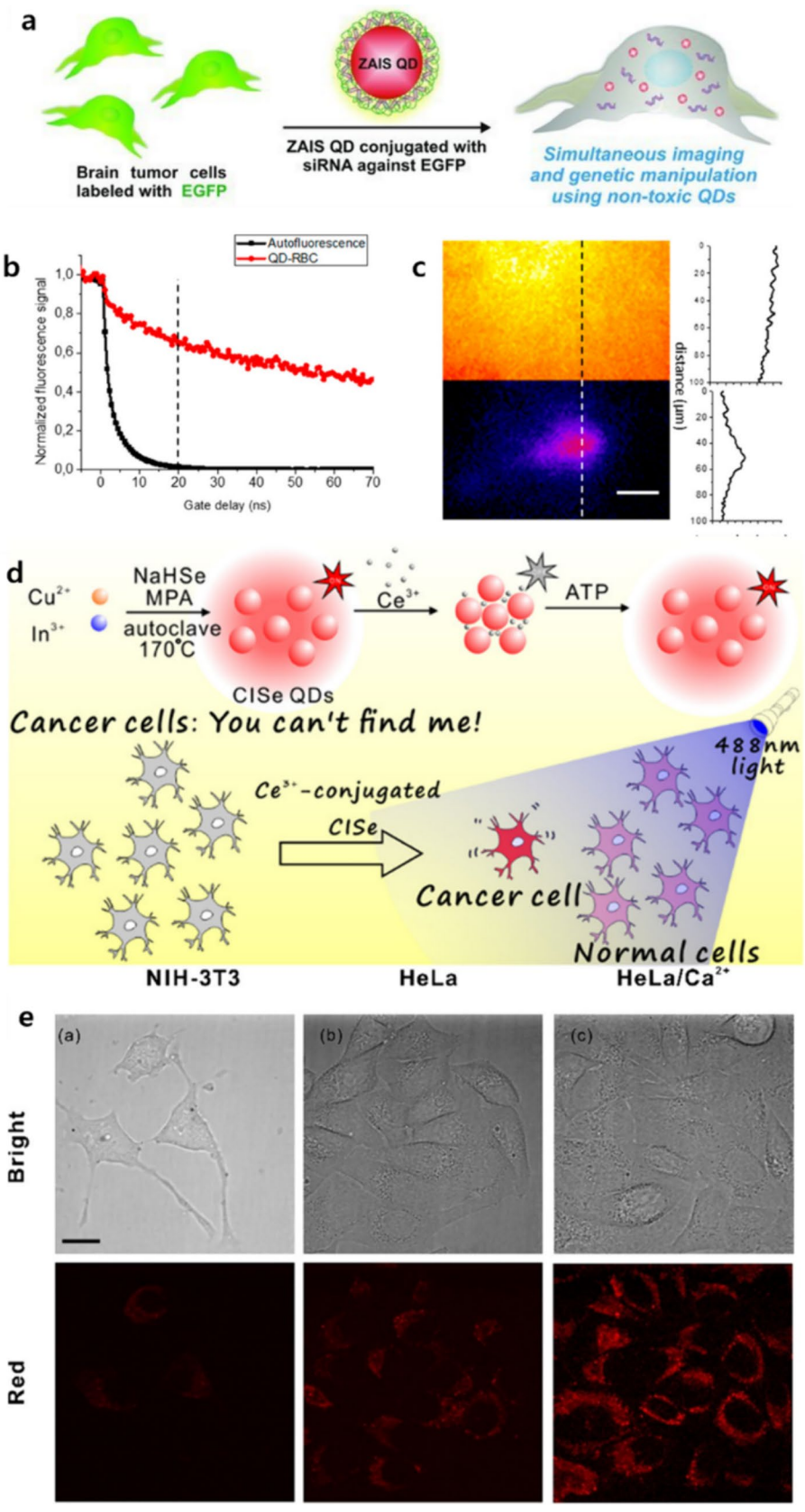

Fig. 13 **a** Delivery of the siRNA against EGFP using ZAIS QD-siRNA conjugates into brain cancer cells overexpressing EGFP. Reproduced with permission [116]. Copyright 2012 Wiley. **b** In vivo autofluorescence (black) and fluorescence of QD-loaded RBC (red) as a function of gate delay (gate duration: 130 ns). The dotted line corresponds to the 20 ns delay selected for the following experiments. **c** In vivo fluorescence image at delay = 0 (top) and 20 ns (bottom), showing a circulating QD-labeled red blood cell (scale bar = 40 μm). Inset: intensity profiles along the dotted line. Reproduced with permission [117]. Copyright 2019 American Chemical Society. **d** Scheme for turn-on type detection of adenosine triphosphate by Ce^{3+}-conjugated CISe QDs. **e** Confocal laser scanning microscopy images of NIH-3T3 cells, HeLa cells, and Ca2+-treated HeLa cells with the Ce^{3+}-conjugated CISe QDs. Scale bar: 24 μm. Reproduced with permission [118]. Copyright 2021 American Chemical Society

control, surface post-treatment, and core/shell structures. Based on the development of these QD synthesis methods, bio- and display applications of non-toxic QDs have been introduced. In bio-applications, NIR-emitting QDs or QDs doped with Mn^{2+} have been used as biosensors and in bio-imaging because of the deep-tissue penetration depth of NIR light. In addition to exploiting their PL properties, QDs have been used for drug delivery owing to their high surface areas. For display applications, InP-based QDs have been commercialized mainly as CCLs, while $AgInS_2$-based QDs are now being developed for use as post-InP QDs. Beyond CCLs, QDs for QLED devices are also being developed, and for this purpose, QD micropatterning techniques, such as inkjet printing and photolithography, are also being developed.

Although a wide variety of high-quality non-toxic QDs have been developed and are currently utilized in various fields, some challenges still remain. The first challenge is the stability of the QDs. In the case of bio-applications, the surface of the QDs is modified by functional ligands or silica shells, endowing the QDs with biocompatibility. However, these modifications cause surface degradation, leading to low luminance and stability. In addition, in the case of display applications, non-toxic QDs do not have a long device lifetime when fabricated into QLED devices, especially the short operating time of blue QLEDs, presumably owing to the degradation of the QD by the high current density. Therefore, improving the stability of QD by polymer encapsulation and reducing the operating current density are necessary.

The second challenge is the development of high-quality non-toxic QDs that emit light in the NIR region. In the case of InP, $Ag(InGa)S_2$, and ZnSeTe QDs emitting in the visible region, their high QY and narrow half-widths are expected to be utilized in displays. However, Ag- or Cu-based non-toxic QDs, which emit in the NIR region, have a wide FWHM and low PLQY, limiting their application. Methods to realize this goal include preparing precursor libraries with smoothly tunable reactivities and a new shell structure to enhance narrow-band-edge emission.

The third challenge is the high price of non-toxic QDs. Currently, commercialized QDs are InP-based QDs applied as color-conversion layers in displays. However, InP-based QDs have a cost disadvantage, because they must be synthesized using rare-earth indium and expensive $P(TMS)_3$ precursors. In addition, In-based QDs such as $AgInS_2$ and $CuInS_2$ QDs emitting in the NIR region have been actively utilized in bio-applications. To reduce the precursor costs, identifying chemical synthesis methods for non-toxic QDs from alternative earth-abundant materials or inexpensive precursors remains a challenging task.

In conclusion, considering the progress in the synthesis of QDs and their applications, non-toxic QDs are expected to be applied in high-resolution display devices and advanced biomedical solutions. Moreover, resolving the various issues faced would lead to the successful commercialization of non-toxic QDs in the near future.

Acknowledgements This work was partially supported by a National Research Foundation of Korea (NRF) grant funded by the Korean government (MSIT) (No. RS-2023-00210462) and in part by a Korea Evaluation Institute of Industrial Technology (KEIT) grant funded by the Ministry of Trade, Industry & Energy (MOTIE, Korea) (20015805, Development of material parts and processing technology for post-InP fluorescence quantum dot).

Data availability All data generated or analysed during this study are included in this published article.

References

1. A.P. Alivisatos, Semiconductor clusters, nanocrystals, and quantum dots. Science **271**, 933–937 (1996). https://doi.org/10.1126/science.271.5251.933
2. F.P. García De Arquer, D.V. Talapin, V.I. Klimov, Y. Arakawa, M. Bayer, E.H. Sargent, Semiconductor quantum dots: technological progress and future challenges. Science **373**, eaaz8541 (2021). https://doi.org/10.1126/science.aaz8541
3. J.M. Pietryga, Y.-S. Park, J. Lim, A.F. Fidler, W.K. Bae, S. Brovelli, V.I. Klimov, Spectroscopic and device aspects of nanocrystal quantum dots. Chem. Rev. **116**, 10513–10622 (2016). https://doi.org/10.1021/acs.chemrev.6b00169
4. P. Reiss, M. Carrière, C. Lincheneau, L. Vaure, S. Tamang, Synthesis of semiconductor nanocrystals, focusing on nontoxic and earth-abundant materials. Chem. Rev. **116**, 10731–10819 (2016). https://doi.org/10.1021/acs.chemrev.6b00116
5. H. Lu, G.M. Carroll, N.R. Neale, M.C. Beard, Infrared quantum dots: progress, challenges, and opportunities. ACS Nano (2019). https://doi.org/10.1021/acsnano.8b09815
6. D.V. Talapin, J.-S. Lee, M.V. Kovalenko, E.V. Shevchenko, Prospects of colloidal nanocrystals for electronic and optoelectronic applications. Chem. Rev. **110**, 389–458 (2010). https://doi.org/10.1021/cr900137k
7. I.L. Medintz, H.T. Uyeda, E.R. Goldman, H. Mattoussi, Quantum dot bioconjugates for imaging, labelling and sensing. Nat. Mater. **4**, 435–446 (2005). https://doi.org/10.1038/nmat1390
8. A.A. Guzelian, J.E.B. Katari, A.V. Kadavanich, U. Banin, K. Hamad, E. Juban, A.P. Alivisatos, R.H. Wolters, C.C. Arnold, J.R. Heath, Synthesis of size-selected, surface-passivated InP nanocrystals. J. Phys. Chem. **100**, 7212–7219 (1996). https://doi.org/10.1021/jp953719f
9. J.F. Janik, R.L. Wells, Gallium imide, Ga(NH) 3/2 n, a new polymeric precursor for gallium nitride powders. Chem. Mater. **8**, 2708–2711 (1996). https://doi.org/10.1021/cm960419h
10. D. Battaglia, X. Peng, Formation of high quality InP and InAs nanocrystals in a noncoordinating solvent. Nano Lett. **2**, 1027–1030 (2002). https://doi.org/10.1021/nl025687v
11. S. Adam, D.V. Talapin, H. Borchert, A. Lobo, C. McGinley, A.R.B. De Castro, M. Haase, H. Weller, T. Möller, The effect of nanocrystal surface structure on the luminescence properties: photoemission study of HF-etched InP nanocrystals. J. Chem. Phys. **123**, 084706 (2005). https://doi.org/10.1063/1.2004901
12. S. Haubold, M. Haase, A. Kornowski, H. Weller, Strongly luminescent InP/ZnS core-shell nanoparticles. ChemPhysChem **2**,

331–334 (2001). https://doi.org/10.1002/1439-7641(20010518)2:5%3c331::AID-CPHC331%3e3.0.CO;2-0
13. J. Lim, M. Park, W.K. Bae, D. Lee, S. Lee, C. Lee, K. Char, Highly efficient cadmium-free quantum dot light-emitting diodes enabled by the direct formation of excitons within InP@ZnSeS quantum dots. ACS Nano **7**, 9019–9026 (2013). https://doi.org/10.1021/nn403594j
14. Y.-H. Won, O. Cho, T. Kim, D.-Y. Chung, T. Kim, H. Chung, H. Jang, J. Lee, D. Kim, E. Jang, Highly efficient and stable InP/ZnSe/ZnS quantum dot light-emitting diodes. Nature **575**, 634–638 (2019). https://doi.org/10.1038/s41586-019-1771-5
15. H. Li, W. Zhang, Y. Bian, T.K. Ahn, H. Shen, B. Ji, ZnF_2-assisted synthesis of highly luminescent InP/ZnSe/ZnS quantum dots for efficient and stable electroluminescence. Nano Lett. **22**, 4067–4073 (2022). https://doi.org/10.1021/acs.nanolett.2c00763
16. D. Lee, S. Koh, D.-E. Yoon, S. Lee, W.D. Kim, D. Kim, W.K. Bae, J. Lim, D.C. Lee, Synthesis of InP nanocrystals using triphenyl phosphite as phosphorus source. Korean J. Chem. Eng. **36**, 1518–1526 (2019). https://doi.org/10.1007/s11814-019-0344-5
17. Y.-J. Bai, Z.-G. Liu, X.-G. Xu, D.-L. Cui, X.-P. Hao, X. Feng, Q.-L. Wang, Preparation of InN nanocrystals by solvo-thermal method. J. Cryst. Growth (2002). https://doi.org/10.1016/S0022-0248(02)01292-7
18. C. Wu, T. Li, L. Lei, S. Hu, Y. Liu, Y. Xie, Indium nitride from indium iodide at low temperatures: synthesis and their optical properties. New J. Chem. **29**, 1610 (2005). https://doi.org/10.1039/b510426b
19. M.R. Greenberg, W. Chen, B.N. Pulford, G.A. Smolyakov, Y.-B. Jiang, S.D. Bunge, T.J. Boyle, M. Osinski, Synthesis and characterization of InP and InN colloidal quantum dots. Proc. SPIE **5705**, 68−76 (2005). https://doi.org/10.1117/12.601507
20. P.K.B. Palomaki, E.M. Miller, N.R. Neale, Control of plasmonic and interband transitions in colloidal indium nitride nanocrystals. J. Am. Chem. Soc. **135**, 14142–14150 (2013). https://doi.org/10.1021/ja404599g
21. D. Wen, N. Kirkwood, P. Mulvaney, Synthesis of size-tunable indium nitride nanocrystals. J. Phys. Chem. Lett. **14**, 3669–3676 (2023). https://doi.org/10.1021/acs.jpclett.3c00024
22. K.D. Wegner, S. Pouget, W.L. Ling, M. Carrière, P. Reiss, Gallium – a versatile element for tuning the photoluminescence properties of InP quantum dots. Chem. Commun. **55**, 1663–1666 (2019). https://doi.org/10.1039/C8CC09740B
23. S. Kim, T. Kim, M. Kang, S.K. Kwak, T.W. Yoo, L.S. Park, I. Yang, S. Hwang, J.E. Lee, S.K. Kim, S.-W. Kim, Highly luminescent InP/GaP/ZnS nanocrystals and their application to white light-emitting diodes. J. Am. Chem. Soc. **134**, 3804–3809 (2012). https://doi.org/10.1021/ja210211z
24. V. Srivastava, V. Kamysbayev, L. Hong, E. Dunietz, R.F. Klie, D.V. Talapin, Colloidal chemistry in molten salts: synthesis of luminescent in 1–x Ga x P and In 1–x Ga x as quantum dots. J. Am. Chem. Soc. **140**, 12144–12151 (2018). https://doi.org/10.1021/jacs.8b06971
25. K.-H. Kim, J.-H. Jo, D.-Y. Jo, C.-Y. Han, S.-Y. Yoon, Y. Kim, Y.-H. Kim, Y.H. Ko, S.W. Kim, C. Lee, H. Yang, Cation-exchange-derived InGaP alloy quantum dots toward blue emissivity. Chem. Mater. **32**, 3537–3544 (2020). https://doi.org/10.1021/acs.chemmater.0c00551
26. Y. Du, B. Xu, T. Fu, M. Cai, F. Li, Y. Zhang, Q. Wang, Near-infrared photoluminescent Ag_2S quantum dots from a single source precursor. J. Am. Chem. Soc. **132**, 1470–1471 (2010). https://doi.org/10.1021/ja909490r
27. Y. Zhang, Y. Liu, C. Li, X. Chen, Q. Wang, Controlled synthesis of Ag_2S quantum dots and experimental determination of the exciton bohr radius. J. Phys. Chem. C **118**, 4918–4923 (2014). https://doi.org/10.1021/jp501266d
28. Y. Sung, H.B. Kim, J.H. Kim, Y. Noh, J. Yu, J. Yang, T.H. Kim, J. Oh, Facile ligand exchange of ionic ligand-capped amphiphilic Ag_2S nanocrystals for high conductive thin films. ACS Appl. Mater. Interfaces **16**, 3853–3861 (2024). https://doi.org/10.1021/acsami.3c15472
29. H. Doh, S. Hwang, S. Kim, Size-tunable synthesis of nearly monodisperse Ag_2S nanoparticles and size-dependent fate of the crystal structures upon cation exchange to $AgInS_2$ nanoparticles. Chem. Mater. **28**, 8123–8127 (2016). https://doi.org/10.1021/acs.chemmater.6b04011
30. L. Pan, J. Tu, L. Yang, Z. Tian, Z. Zhang, Photoluminescence enhancement of NIR-II emissive Ag_2S quantum dots via chloride-mediated growth and passivation. Adv. Opt. Mater. **10**, 2102806 (2022). https://doi.org/10.1002/adom.202102806
31. Y. Sung, W. Lee, E. Lee, Y.H. Ko, S. Kim, Ion-pair ligand-assisted surface stoichiometry control of Ag_2S nanocrystals. Chem. Mater. **34**, 9945–9954 (2022). https://doi.org/10.1021/acs.chemmater.2c02038
32. A. Sahu, L. Qi, M.S. Kang, D. Deng, D.J. Norris, Facile synthesis of silver Chalcogenide (Ag_2E; E = Se, S, Te) semiconductor nanocrystals. J. Am. Chem. Soc. **133**, 6509–6512 (2011). https://doi.org/10.1021/ja200012e
33. C.-N. Zhu, P. Jiang, Z.-L. Zhang, D.-L. Zhu, Z.-Q. Tian, D.-W. Pang, Ag_2Se quantum dots with tunable emission in the second near-infrared window. ACS Appl. Mater. Interfaces **5**, 1186–1189 (2013). https://doi.org/10.1021/am303110x
34. L.-J. Shi, C.-N. Zhu, H. He, D.-L. Zhu, Z.-L. Zhang, D.-W. Pang, Z.-Q. Tian, Near-infrared Ag_2Se quantum dots with distinct absorption features and high fluorescence quantum yields. RSC Adv. **6**, 38183–38186 (2016). https://doi.org/10.1039/C6RA04987G
35. B. Dong, C. Li, G. Chen, Y. Zhang, Y. Zhang, M. Deng, Q. Wang, Facile synthesis of highly photoluminescent Ag_2Se quantum dots as a new fluorescent probe in the second near-infrared window for in vivo imaging. Chem. Mater. **25**, 2503–2509 (2013). https://doi.org/10.1021/cm400812v
36. M. Yarema, S. Pichler, M. Sytnyk, R. Seyrkammer, R.T. Lechner, G. Fritz-Popovski, D. Jarzab, K. Szendrei, R. Resel, O. Korovyanko, M.A. Loi, O. Paris, G. Hesser, W. Heiss, Infrared emitting and photoconducting colloidal silver chalcogenide nanocrystal quantum dots from a silylamide-promoted synthesis. ACS Nano **5**, 3758–3765 (2011). https://doi.org/10.1021/nn2001118
37. H. Yang, R. Li, Y. Zhang, M. Yu, Z. Wang, X. Liu, W. You, D. Tu, Z. Sun, R. Zhang, X. Chen, Q. Wang, Colloidal alloyed quantum dots with enhanced photoluminescence quantum yield in the NIR-II window. J. Am. Chem. Soc. **143**, 2601–2607 (2021). https://doi.org/10.1021/jacs.0c13071
38. Z. Sun, C. Liu, H. Yang, X. Yang, Y. Zhang, H. Lin, Y. Li, Q. Wang, AgAuSe quantum dots with absolute photoluminescence quantum yield of 87.2%: the effect of capping ligand chain length. Nano Res. **15**, 8555–8563 (2022). https://doi.org/10.1007/s12274-022-4417-0
39. Y.-T. Yang, Y.-Z. Guo, Z.-C. Shen, J.-L. Liu, R. Yuan, Y.-Q. Chai, AgAuS quantum dots as a highly efficient near-infrared electrochemiluminescence emitter for the ultrasensitive detection of MicroRNA. Anal. Chem. **95**, 9314–9322 (2023). https://doi.org/10.1021/acs.analchem.3c01346
40. S.P. Hong, H.K. Park, J.H. Oh, H. Yang, Y.R. Do, Comparisons of the structural and optical properties of o-AgInS2, t-AgInS2, and c-AgIn5S8 nanocrystals and their solid-solution nanocrystals with ZnS. J. Mater. Chem. **22**, 18939 (2012). https://doi.org/10.1039/c2jm33879c
41. T. Torimoto, T. Adachi, K. Okazaki, M. Sakuraoka, T. Shibayama, B. Ohtani, A. Kudo, S. Kuwabata, Facile synthesis of $ZnS-AgInS_2$ solid solution nanoparticles for a color-adjustable

luminophore. J. Am. Chem. Soc. **129**, 12388–12389 (2007). https://doi.org/10.1021/ja0750470
42. X. Tang, W.B.A. Ho, J.M. Xue, Synthesis of Zn-doped $AgInS_2$ nanocrystals and their fluorescence properties. J. Phys. Chem. C **116**, 9769–9773 (2012). https://doi.org/10.1021/jp207711p
43. T. Uematsu, K. Wajima, D.K. Sharma, S. Hirata, T. Yamamoto, T. Kameyama, M. Vacha, T. Torimoto, S. Kuwabata, Narrow band-edge photoluminescence from AgInS2 semiconductor nanoparticles by the formation of amorphous III–VI semiconductor shells. NPG Asia Mater. **10**, 713–726 (2018). https://doi.org/10.1038/s41427-018-0067-9
44. R. Xie, M. Rutherford, X. Peng, Formation of high-quality I–III−VI semiconductor nanocrystals by tuning relative reactivity of cationic precursors. J. Am. Chem. Soc. **131**, 5691–5697 (2009). https://doi.org/10.1021/ja9005767
45. B. Mao, C.-H. Chuang, C. McCleese, J. Zhu, C. Burda, near-infrared emitting $AgInS_2$/ZnS nanocrystals. J. Phys. Chem. C **118**, 13883–13889 (2014). https://doi.org/10.1021/jp500872w
46. J.-H. Kim, B.-Y. Kim, E.-P. Jang, S.-Y. Yoon, K.-H. Kim, Y.R. Do, H. Yang, Synthesis of widely emission-tunable Ag–Ga–S and its quaternary derivative quantum dots. Chem. Eng. J. **347**, 791–797 (2018). https://doi.org/10.1016/j.cej.2018.04.167
47. W. Hoisang, T. Uematsu, T. Torimoto, S. Kuwabata, Surface ligand chemistry on quaternary Ag(In x Ga 1–x)S 2 semiconductor quantum dots for improving photoluminescence properties. Nanoscale Adv. **4**, 849–857 (2022). https://doi.org/10.1039/D1NA00684C
48. T. Uematsu, M. Tepakidareekul, T. Hirano, T. Torimoto, S. Kuwabata, Facile high-yield synthesis of Ag–In–Ga–S quaternary quantum dots and coating with gallium sulfide shells for narrow band-edge emission. Chem. Mater. **35**, 1094–1106 (2023). https://doi.org/10.1021/acs.chemmater.2c03023
49. S.L. Castro, S.G. Bailey, R.P. Raffaelle, K.K. Banger, A.F. Hepp, Synthesis and characterization of colloidal $CuInS_2$ nanoparticles from a molecular single-source precursor. J. Phys. Chem. B **108**, 12429–12435 (2004). https://doi.org/10.1021/jp049107p
50. L. Li, A. Pandey, D.J. Werder, B.P. Khanal, J.M. Pietryga, V.I. Klimov, Efficient synthesis of highly luminescent copper indium sulfide-based core/shell nanocrystals with surprisingly long-lived emission. J. Am. Chem. Soc. **133**, 1176–1179 (2011). https://doi.org/10.1021/ja108261h
51. C. Xia, J.D. Meeldijk, H.C. Gerritsen, C. De Mello Donega, Highly luminescent water-dispersible NIR-emitting wurtzite CuInS2/ZnS core/shell colloidal quantum dots. Chem. Mater. **29**, 4940–4951 (2017). https://doi.org/10.1021/acs.chemmater.7b01258
52. P.M. Allen, M.G. Bawendi, Ternary I−III−VI quantum dots luminescent in the red to near-infrared. J. Am. Chem. Soc. **130**, 9240–9241 (2008). https://doi.org/10.1021/ja8036349
53. E. Cassette, T. Pons, C. Bouet, M. Helle, L. Bezdetnaya, F. Marchal, B. Dubertret, Synthesis and characterization of near-infrared Cu−In−Se/ZnS core/shell quantum dots for in vivo imaging. Chem. Mater. **22**, 6117–6124 (2010). https://doi.org/10.1021/cm101881b
54. O. Yarema, D. Bozyigit, I. Rousseau, L. Nowack, M. Yarema, W. Heiss, V. Wood, Highly luminescent, size- and shape-tunable copper indium selenide based colloidal nanocrystals. Chem. Mater. **25**, 3753–3757 (2013). https://doi.org/10.1021/cm402306q
55. J. Ning, Y. Xiong, F. Huang, Z. Duan, S.V. Kershaw, A.L. Rogach, Growth of multinary copper-based sulfide shells on $CuInSe_2$ nanocrystals for significant improvement of their near-infrared emission. Chem. Mater. **32**, 7842–7849 (2020). https://doi.org/10.1021/acs.chemmater.0c02500
56. J. Joo, H.B. Na, T. Yu, J.H. Yu, Y.W. Kim, F. Wu, J.Z. Zhang, T. Hyeon, Generalized and facile synthesis of semiconducting metal sulfide nanocrystals. J. Am. Chem. Soc. **125**, 11100–11105 (2003). https://doi.org/10.1021/ja0357902
57. Y. Zhao, Y. Zhang, H. Zhu, G.C. Hadjipanayis, J.Q. Xiao, Low-temperature synthesis of hexagonal (wurtzite) ZnS nanocrystals. J. Am. Chem. Soc. **126**, 6874–6875 (2004). https://doi.org/10.1021/ja048650g
58. L.S. Li, N. Pradhan, Y. Wang, X. Peng, High quality ZnSe and ZnS nanocrystals formed by activating zinc carboxylate precursors. Nano Lett. **4**, 2261–2264 (2004). https://doi.org/10.1021/nl048650e
59. E. Bennett, M.W. Greenberg, A.J. Jordan, L.S. Hamachi, S. Banerjee, S.J.L. Billinge, J.S. Owen, Size dependent optical properties and structure of ZnS nanocrystals prepared from a library of thioureas. Chem. Mater. **34**, 706–717 (2022). https://doi.org/10.1021/acs.chemmater.1c03432
60. M.A. Hines, P. Guyot-Sionnest, Bright UV-blue luminescent colloidal ZnSe nanocrystals. J. Phys. Chem. B **102**, 3655–3657 (1998). https://doi.org/10.1021/jp9810217
61. B. Ji, S. Koley, I. Slobodkin, S. Remennik, U. Banin, ZnSe/ZnS core/shell quantum dots with superior optical properties through thermodynamic shell growth. Nano Lett. **20**, 2387–2395 (2020). https://doi.org/10.1021/acs.nanolett.9b05020
62. Z. Long, M. Liu, X. Wu, K. Gu, G. Yang, Z. Chen, Y. Liu, R. Liu, H. Zhong, A reactivity-controlled epitaxial growth strategy for synthesizing large nanocrystals. Nat. Synth. **2**, 296–304 (2023). https://doi.org/10.1038/s44160-022-00210-5
63. C. Li, K. Nishikawa, M. Ando, H. Enomoto, N. Murase, Synthesis of Cd-free water-soluble $ZnSe_{1-x}Te_x$ nanocrystals with high luminescence in the blue region. J. Colloid Interface Sci. **321**, 468–476 (2008). https://doi.org/10.1016/j.jcis.2008.02.009
64. E.-P. Jang, C.-Y. Han, S.-W. Lim, J.-H. Jo, D.-Y. Jo, S.-H. Lee, S.-Y. Yoon, H. Yang, Synthesis of alloyed ZnSeTe Quantum dots as bright, color-pure blue emitters. ACS Appl. Mater. Interfaces **11**, 46062–46069 (2019). https://doi.org/10.1021/acsami.9b14763
65. S.-H. Lee, C.-Y. Han, S.-W. Song, D.-Y. Jo, J.-H. Jo, S.-Y. Yoon, H.-M. Kim, S. Hong, J.Y. Hwang, H. Yang, ZnSeTe quantum dots as an alternative to InP and their high-efficiency electroluminescence. Chem. Mater. **32**, 5768–5775 (2020). https://doi.org/10.1021/acs.chemmater.0c01596
66. T. Kim, K.-H. Kim, S. Kim, S.-M. Choi, H. Jang, H.-K. Seo, H. Lee, D.-Y. Chung, E. Jang, Efficient and stable blue quantum dot light-emitting diode. Nature **586**, 385–389 (2020). https://doi.org/10.1038/s41586-020-2791-x
67. H.-S. Kim, E.J. Kim, J. Kim, The optimal color space for realistic color reproduction in virtual reality content design. Electronics **12**, 4630 (2023). https://doi.org/10.3390/electronics12224630
68. H. Cho, C. Kang, B.-H. Kwon, S. Choi, C.W. Joo, H. Lee, Luminance compensation in top-emitting organic light-emitting diodes with high color purity as quantum dots using horizontal dipole orientation. Org. Electron. **87**, 105945 (2020). https://doi.org/10.1016/j.orgel.2020.105945
69. Y. Li, Z. Chen, B. Kristal, Y. Zhang, D. Li, G. Yu, X. Wang, L. Wang, Y. Shi, Z. Wang, Y. Chen, J. Yu, Y. He, 80–1: invited paper: developing AMQLED technology for display applications. SID Symp. Dig. Tech. Pap. **49**, 1076–1079 (2018). https://doi.org/10.1002/sdtp.12130
70. S. Choi, J. Moon, H. Cho, B.-H. Kwon, N.S. Cho, H. Lee, Partially pyridine-functionalized quantum dots for efficient red, green, and blue light-emitting diodes. J. Mater. Chem. C **7**, 3429–3435 (2019). https://doi.org/10.1039/C8TC04414G
71. H. Park, D. Hahm, H. Cho, J.-W. Shin, C. Kang, D.-H. Ahn, C.W. Joo, B.-H. Kwon, K. Kim, J.Y. Kim, B.G. Jeong, N.S. Cho, W.K. Bae, J. Lee, S. Choi, Efficient quantum dot color conversion layer with mixed spherical/rod-shaped scattering particles. ACS Appl.

Opt. Mater. **1**, 289–297 (2023). https://doi.org/10.1021/acsaom.2c00054
72. H.J. Lee, S. Im, D. Jung, K. Kim, J.A. Chae, J. Lim, J.W. Park, D. Shin, K. Char, B.G. Jeong, J.-S. Park, E. Hwang, D.C. Lee, Y.-S. Park, H.-J. Song, J.H. Chang, W.K. Bae, Coherent heteroepitaxial growth of I-III-VI2 Ag(In, Ga)S2 colloidal nanocrystals with near-unity quantum yield for use in luminescent solar concentrators. Nat. Commun. **14**, 3779 (2023). https://doi.org/10.1038/s41467-023-39509-y
73. W. Hoisang, T. Uematsu, T. Torimoto, S. Kuwabata, Luminescent quaternary Ag(In x Ga 1–x)S 2 /GaS y core/shell quantum dots prepared using dithiocarbamate compounds and photoluminescence recovery via post treatment. Inorg. Chem. **60**, 13101–13109 (2021). https://doi.org/10.1021/acs.inorgchem.1c01513
74. H. Kim, M. Ryu, J.H.J. Cha, H.S. Kim, T. Jeong, J. Jang, Ten micrometer pixel, quantum dots color conversion layer for high resolution and full color active matrix micro-LED display. J. Soc. Inf. Disp. **27**, 347–353 (2019). https://doi.org/10.1002/jsid.782
75. T. Xuan, S. Shi, L. Wang, H.-C. Kuo, R.-J. Xie, Inkjet-printed quantum dot color conversion films for high-resolution and full-color micro light-emitting diode displays. J. Phys. Chem. Lett. **11**, 5184–5191 (2020). https://doi.org/10.1021/acs.jpclett.0c01451
76. E. Lee, R. Tangirala, A. Smith, A. Carpenter, C. Hotz, H. Kim, J. Yurek, T. Miki, S. Yoshihara, T. Kizaki, A. Ishizuka, I. Kiyoto, 41–5: *invited paper:* quantum dot conversion layers through inkjet printing. SID Symp. Dig. Tech. Pap. **49**, 525–527 (2018). https://doi.org/10.1002/sdtp.12452
77. H.C. Kim, C. Yoon, Y.-G. Song, Y.-J. Kim, K. Lee, Enhancing performance of quantum dot-based light emitting diodes by using poly(methyl methacrylate)@quantum dot hybrid particles. Korean J. Chem. Eng. **32**, 563–566 (2015). https://doi.org/10.1007/s11814-015-0008-z
78. W.K. Bae, J. Lim, Nanostructured colloidal quantum dots for efficient electroluminescence devices. Korean J. Chem. Eng. **36**, 173–185 (2019). https://doi.org/10.1007/s11814-018-0193-7
79. D. Hahm, J.H. Chang, B.G. Jeong, P. Park, J. Kim, S. Lee, J. Choi, W.D. Kim, S. Rhee, J. Lim, D.C. Lee, C. Lee, K. Char, W.K. Bae, Design principle for bright, robust, and color-pure InP/ZnSe x S 1–x/ZnS heterostructures. Chem. Mater. **31**, 3476–3484 (2019). https://doi.org/10.1021/acs.chemmater.9b00740
80. C. Ippen, B. Newmeyer, D. Zehnder, D. Kim, D. Barrera, C. Hotz, R. Ma, 58–1: invited paper: progress in high-efficiency heavy-metal-free QD-LED development. SID Symp. Dig. Tech. Pap. **51**, 858–861 (2020). https://doi.org/10.1002/sdtp.14005
81. C.-Y. Han, S.-H. Lee, S.-W. Song, S.-Y. Yoon, J.-H. Jo, D.-Y. Jo, H.-M. Kim, B.-J. Lee, H.-S. Kim, H. Yang, More than 9% efficient ZnSeTe quantum dot-based blue electroluminescent devices. ACS Energy Lett. **5**, 1568–1576 (2020). https://doi.org/10.1021/acsenergylett.0c00638
82. Cadmium-free quantum dot light emitting devices: energy-transfer realizing pure blue emission, (2024). https://opg.optica.org/ol/abstract.cfm?uri=ol-38-1-7. Accessed May 16, 2024
83. A. Wang, H. Shen, S. Zang, Q. Lin, H. Wang, L. Qian, J. Niu, L.S. Li, Bright, efficient, and color-stable violet ZnSe-based quantum dot light-emitting diodes. Nanoscale **7**, 2951–2959 (2015). https://doi.org/10.1039/C4NR06593J
84. M. Gao, H. Yang, H. Shen, Z. Zeng, F. Fan, B. Tang, J. Min, Y. Zhang, Q. Hua, L.S. Li, B. Ji, Z. Du, Bulk-like ZnSe quantum dots enabling efficient ultranarrow blue light-emitting diodes. Nano Lett. **21**, 7252–7260 (2021). https://doi.org/10.1021/acs.nanolett.1c02284
85. J. Lim, W.K. Bae, D. Lee, M.K. Nam, J. Jung, C. Lee, K. Char, S. Lee, InP@ZnSeS, Core@Composition gradient shell quantum dots with enhanced stability. Chem. Mater. **23**, 4459–4463 (2011). https://doi.org/10.1021/cm201550w
86. H. Moon, W. Lee, J. Kim, D. Lee, S. Cha, S. Shin, H. Chae, Composition-tailored ZnMgO nanoparticles for electron transport layers of highly efficient and bright InP-based quantum dot light emitting diodes. Chem. Commun. **55**, 13299–13302 (2019). https://doi.org/10.1039/C9CC06882A
87. W.-C. Chao, T.-H. Chiang, Y.-C. Liu, Z.-X. Huang, C.-C. Liao, C.-H. Chu, C.-H. Wang, H.-W. Tseng, W.-Y. Hung, P.-T. Chou, High efficiency green InP quantum dot light-emitting diodes by balancing electron and hole mobility. Commun. Mater. **2**, 1–10 (2021). https://doi.org/10.1038/s43246-021-00203-5
88. H. Zhang, N. Hu, Z. Zeng, Q. Lin, F. Zhang, A. Tang, Y. Jia, L.S. Li, H. Shen, F. Teng, Z. Du, High-efficiency green InP quantum dot-based electroluminescent device comprising thick-shell quantum dots. Adv. Opt. Mater. **7**, 1801602 (2019). https://doi.org/10.1002/adom.201801602
89. T. Lee, D. Hahm, K. Kim, W.K. Bae, C. Lee, J. Kwak, Highly efficient and bright inverted top-emitting InP quantum dot light-emitting diodes introducing a hole-suppressing interlayer. Small **15**, 1905162 (2019). https://doi.org/10.1002/smll.201905162
90. D. Li, J. Feng, Y. Zhu, Z. Lu, C. Pei, Z. Chen, Y. Li, X. Li, X. Xu, Enhanced efficiency of top-emission InP-based green quantum dot light-emitting diodes with optimized angular distribution. Nano Res. **14**, 4243–4249 (2021). https://doi.org/10.1007/s12274-021-3596-4
91. J.-H. Jo, J.-H. Kim, K.-H. Lee, C.-Y. Han, E.-P. Jang, Y.R. Do, H. Yang, High-efficiency red electroluminescent device based on multishelled InP quantum dots. Opt. Lett. **41**, 3984–3987 (2016). https://doi.org/10.1364/OL.41.003984
92. Y. Li, X. Hou, X. Dai, Z. Yao, L. Lv, Y. Jin, X. Peng, Stoichiometry-controlled InP-based quantum dots: synthesis, photoluminescence, and electroluminescence. J. Am. Chem. Soc. **141**, 6448–6452 (2019). https://doi.org/10.1021/jacs.8b12908
93. F. Cao, S. Wang, F. Wang, Q. Wu, D. Zhao, X. Yang, A layer-by-layer growth strategy for large-size InP/ZnSe/ZnS core-shell quantum dots enabling high-efficiency light-emitting diodes. Chem. Mater. **30**, 8002–8007 (2018). https://doi.org/10.1021/acs.chemmater.8b03671
94. M.G. Han, Y. Lee, H. Kwon, H. Lee, T. Kim, Y.-H. Won, E. Jang, InP-based quantum dot light-emitting diode with a blended emissive layer. ACS Energy Lett. **6**, 1577–1585 (2021). https://doi.org/10.1021/acsenergylett.1c00351
95. J.E. Yeom, D.H. Shin, R. Lampande, Y.H. Jung, N.N. Mude, J.H. Park, J.H. Kwon, Good charge balanced inverted red InP/ZnSe/ZnS-quantum dot light-emitting diode with new high mobility and deep HOMO level hole transport layer. ACS Energy Lett. **5**, 3868–3875 (2020). https://doi.org/10.1021/acsenergylett.0c02193
96. G. Hong, J.T. Robinson, Y. Zhang, S. Diao, A.L. Antaris, Q. Wang, H. Dai, In vivo fluorescence imaging with Ag_2S quantum dots in the second near-infrared region. Angew. Chem. **124**, 9956–9959 (2012). https://doi.org/10.1002/ange.201206059
97. C. Li, F. Li, Y. Zhang, W. Zhang, X.-E. Zhang, Q. Wang, Real-time monitoring surface chemistry-dependent in vivo behaviors of protein nanocages via encapsulating an NIR-II Ag_2S quantum dot. ACS Nano **9**, 12255–12263 (2015). https://doi.org/10.1021/acsnano.5b05503
98. Y. Zhang, H. Yang, X. An, Z. Wang, X. Yang, M. Yu, R. Zhang, Z. Sun, Q. Wang, Controlled synthesis of Ag_2Te@Ag_2S core-shell quantum dots with enhanced and tunable fluorescence in the second near-infrared window. Small **16**, 2001003 (2020). https://doi.org/10.1002/smll.202001003
99. Q. Ren, Y. Ma, S. Zhang, L. Ga, J. Ai, One-step synthesis of water-soluble silver sulfide quantum dots and their application to

bioimaging. ACS Omega **6**, 6361–6367 (2021). https://doi.org/10.1021/acsomega.0c06276
100. Q. Wu, M. Zhou, J. Shi, Q. Li, M. Yang, Z. Zhang, Synthesis of water-soluble Ag_2S quantum dots with fluorescence in the second near-infrared window for turn-on detection of Zn(II) and Cd(II). Anal. Chem. (2017). https://doi.org/10.1021/acs.analchem.7b00777
101. Q. Wen, Y. Zhang, C. Li, S. Ling, X. Yang, G. Chen, Y. Yang, Q. Wang, NIR-II fluorescent self-assembled peptide nanochain for ultrasensitive detection of peritoneal metastasis. Angew. Chem. Int. Ed. **58**, 11001–11006 (2019). https://doi.org/10.1002/anie.201905643
102. R. Thakar, Y. Chen, P.T. Snee, Efficient emission from core/(doped) shell nanoparticles: applications for chemical sensing. Nano Lett. **7**, 3429–3432 (2007). https://doi.org/10.1021/nl071916
103. J. Xue, Y. Ye, F. Medina, L. Martinez, S.A. Lopez-Rivera, W. Giriat, Temperature evolution of the 2.1eV band in the $Zn_{1-x}Mn_xSe$ system for low concentration. J. Lumin. **78**, 173–178 (1998). https://doi.org/10.1016/S0022-2313(98)00003-9
104. J. Xue, H. Dong, L. Ji, Y. Wang, J. Zhang, Peptide-functionalized ZnSe: Mn quantum dots as fluorescent probes for accurate localization of hidden dental lesion sites. ACS Appl. Nano Mater. **6**, 14431–14438 (2023). https://doi.org/10.1021/acsanm.3c02446
105. D. Zhu, Y. Chen, L. Jiang, J. Geng, J. Zhang, J.-J. Zhu, Manganese-doped ZnSe quantum dots as a probe for time-resolved fluorescence detection of 5-fluorouracil. Anal. Chem. **83**, 9076–9081 (2011). https://doi.org/10.1021/ac202101u
106. Z. Quan, Z. Wang, P. Yang, J. Lin, J. Fang, Synthesis and characterization of high-quality ZnS, ZnS:Mn^{2+}, and ZnS:Mn^{2+}/ZnS (core/shell) luminescent nanocrystals. Inorg. Chem. **46**, 1354–1360 (2007). https://doi.org/10.1021/ic061917n
107. Z.U. Khan, M.K. Uchiyama, L.U. Khan, E.M. Ramos-Sanchez, L.C. Reis, M. Nakamura, H. Goto, A.O. De Souza, K. Araki, H.F. Brito, M. Gidlund, Orange-emitting ZnSe:Mn^{2+} quantum dots as nanoprobes for macrophages. ACS Appl. Nano Mater. **3**, 10399–10410 (2020). https://doi.org/10.1021/acsanm.0c02242
108. X. Cai, Y. Luo, W. Zhang, D. Du, Y. Lin, pH-sensitive ZnO quantum dots-doxorubicin nanoparticles for lung cancer targeted drug delivery. ACS Appl. Mater. Interfaces **8**, 22442–22450 (2016). https://doi.org/10.1021/acsami.6b04933
109. S. Tamang, C. Lincheneau, Y. Hermans, S. Jeong, P. Reiss, Chemistry of InP nanocrystal syntheses. Chem. Mater. **28**, 2491–2506 (2016). https://doi.org/10.1021/acs.chemmater.5b05044
110. P. Roy, M. Virmani, P.P. Pillai, Blue-emitting InP quantum dots participate in an efficient resonance energy transfer process in water. Chem. Sci. **14**, 5167–5176 (2023). https://doi.org/10.1039/D3SC00164D
111. Y. Xu, Y. Lv, R. Wu, J. Li, H. Shen, H. Yang, H. Zhang, L.S. Li, Sensitive immunoassay based on biocompatible and robust silica-coated Cd-free InP-based quantum dots. Inorg. Chem. **60**, 6503–6513 (2021). https://doi.org/10.1021/acs.inorgchem.1c00304
112. G. Lin, T. Chen, Y. Pan, Z. Yang, L. Li, K. Yong, X. Wang, J. Wang, Y. Chen, W. Jiang, S. Weng, X. Huang, J. Kuang, G. Xu, Biodistribution and acute toxicity of cadmium-free quantum dots with different surface functional groups in mice following intratracheal inhalation. Nanotheranostics **4**, 173–183 (2020). https://doi.org/10.7150/ntno.42786
113. T. Kameyama, H. Yamauchi, T. Yamamoto, T. Mizumaki, H. Yukawa, M. Yamamoto, S. Ikeda, T. Uematsu, Y. Baba, S. Kuwabata, T. Torimoto, Tailored photoluminescence properties of Ag(In, Ga)Se_2 quantum dots for near-infrared in vivo imaging. ACS Appl. Nano Mater. **3**, 3275–3287 (2020). https://doi.org/10.1021/acsanm.9b02608
114. X. Long, F. Zhang, Y. He, S. Hou, B. Zhang, G. Zou, Promising anodic electrochemiluminescence of nontoxic core/shell CuInS2/ZnS nanocrystals in aqueous medium and its biosensing potential. Anal. Chem. **90**, 3563–3569 (2018). https://doi.org/10.1021/acs.analchem.8b00006
115. K. Qi, Y. Wang, R. Wang, D. Wu, G.-D. Li, Facile synthesis of homogeneous $CuInS_2$ quantum dots with tunable near-infrared emission. J. Mater. Chem. C **4**, 1895–1899 (2016). https://doi.org/10.1039/C5TC04232A
116. P. Subramaniam, S.J. Lee, S. Shah, S. Patel, V. Starovoytov, K.-B. Lee, Generation of a library of non-toxic quantum dots for cellular imaging and siRNA delivery. Adv. Mater. **24**, 4014–4019 (2012). https://doi.org/10.1002/adma.201201019
117. T. Pons, S. Bouccara, V. Loriette, N. Lequeux, S. Pezet, A. Fragola, In vivo imaging of single tumor cells in fast-flowing bloodstream using near-infrared quantum dots and time-gated imaging. ACS Nano **13**, 3125–3131 (2019). https://doi.org/10.1021/acsnano.8b08463
118. J. Chen, L. Zhang, S. Li, F.-L. Jiang, P. Jiang, Y. Liu, Cu-deficient CuInSe quantum dots for "turn-on" detection of adenosine triphosphate in living cells. ACS Appl. Nano Mater. **4**, 6057–6066 (2021). https://doi.org/10.1021/acsanm.1c00831